AIAA JOURNAL
Vol. 47, No. 3, March 2009

Impact Response of Titanium and Titanium Boride Monolithic and Functionally Graded Composite Plates

Reid A. Larson,* Anthony N. Palazotto,† and Hugh E. Gardenier‡
Air Force Institute of Technology, Wright–Patterson Air Force Base, Ohio 45433

DOI: 10.2514/1.38577

Functionally graded materials have gained significant interest within the research community in recent years. Functionally graded materials are advanced composites in which local material properties are tailored to suit application requirements by altering the volume fraction ratios of two or more constituents. In this article, the behavior of metal–ceramic functionally graded material plates under low-velocity, medium-energy impact loading is considered using experimental and computational techniques. A series of impact tests were conducted on monolithic and functionally graded plates composed of titanium and titanium boride. The tests were performed using a vertical drop test apparatus in which highly controlled impacts of up to 108 J were delivered to the center of the top surface of each plate. The opposing bottom surface of each plate was instrumented with strain gauges wired into a high-speed data acquisition system to collect strain histories throughout the duration of the impact event. A sophisticated finite element model of the test was constructed to simulate the conditions of the experiments. Two distinct material models were used in the finite element analyses to study the monolithic and graded plates. The first model used analytical expressions based on the local volume fractions of the constituents to generate homogenized-material properties for the mixtures of titanium and titanium boride. The second model randomly distributed cells containing titanium elements and titanium boride elements constrained to satisfy local volume fraction ratios in the monolithic and graded specimens. The strain histories from the experiments were compared with the analogous solutions from the finite element model analyses to validate the computational models used in the study. Specifically, analyses with respect to historical trends, maximum strain magnitudes, and strain-rate effects were performed to gain insight into the impact response of the plate structures. The key contribution is validation of functionally graded material models and a computational framework for studying the impact response of functionally graded material plates as a foundation for investigations of more severe impact loads.

Nomenclature

E = elastic modulus
G = shear modulus
K = bulk modulus
V^f = volume fraction
ν = Poisson's ratio
ρ = density

I. Introduction

FUNCTIONALLY graded materials (FGMs) are advanced composites with mechanical properties that vary continuously through a given dimension. The property variation can be accomplished by chemically or mechanically treating a single material locally to alter its characteristics or by varying the volume fraction ratio of two or more constituents along a given dimension. FGMs have generated a great deal of interest in recent years due to their flexibility for use in a wide variety of environments, including those structural applications in which extreme thermal and corrosion resistance are required [1]. In this article, the response of metal–ceramic functionally graded plates subject to impact loading is studied, both experimentally and computationally.

Functionally graded materials, in the general sense, have been available for centuries; in the sense of specially tailored engineering materials, the majority of research into these composites has occurred over the previous two decades. Suresh and Mortensen [1] provided a comprehensive literature review of the state of the art of FGMs dated before 1998, and Birman and Byrd [2] compiled another extensive literature review covering FGM research from 1997 to 2007. Selected works pertinent to this investigation will be highlighted here. Lambros et al. [3,4] developed an inexpensive method for constructing polymer-based FGMs by treating a polyethylene derivative with ultraviolet light. Parameswaran and Shukla [5] developed another inexpensive technique for constructing FGMs by combining aluminum silicate spheres in a polyester resin matrix in which the volume fraction of the spheres was locally tailored to provide the property gradient. These methods can be desirable given the inherent cost and availability of FGM specimens. Reddy et al. [6–9], Loy et al. [10], and Pradhan et al. [11] have studied the behavior of a wide variety of FGM plate configurations under static and dynamic loading, as have others in the field [12–16]. To date, only a few researchers have given consideration to studying impact response and wave propagation in functionally graded composites. Gong et al. [17] studied the low-velocity impact of FGM cylinders with various grading configurations. Bruck [18] developed a technique to manage stress waves in discrete and continuously graded FGMs in one dimension. Li et al. [19] first studied FGM circular plates under dynamic pressures simulating an impact load with a specific metal–ceramic system and using a rate-dependent constitutive relation they developed. Banks-Sills et al. [20] also studied an FGM system under dynamic pressures of various temporal applications. These works were all performed using analytical and computational techniques, but none of them were compared with physical or experimental data given the fact that very little test data of any kind associated with functionally graded composites can be found in the literature. This is due to 1) the difficulty of manufacturing FGMs, 2) the limited availability of such materials in industry and academia, and 3) the high cost associated with producing them.

Presented as Paper 1744 at the 49th AIAA/ASME/ASCE/AHS/ASC Structures, Structural Dynamics, and Materials Conference, Schaumburg, IL, 7–10 April 2008; received 15 May 2008; revision received 10 November 2008; accepted for publication 17 November 2008.

*Graduate Student, Department of Aeronautics & Astronautics. Member AIAA.

†Professor of Aerospace Engineering, Department of Aeronautics & Astronautics. Fellow AIAA.

‡Graduate Student, Department of Aeronautics & Astronautics.

The FGM system used exclusively in this research is a titanium–titanium-boride system developed by BAE Systems Advanced Ceramics in Vista, California. BAE Systems uses a proprietary "reaction sintering" process to produce Ti–TiB FGMs and monolithic composites. Commercially pure titanium (Ti) and titanium diboride (TiB_2) are combined in powder form in a graphite die according to prescribed volume fractions through the plate thickness. A catalyzing agent is applied to the construction, and the powders are subjected to extreme temperature (near the melting point of titanium) and pressure in a vacuum or inert gas environment. The catalyzing agent reacts with the titanium and titanium diboride powders to form titanium boride (TiB) that crystallizes in a needle morphology. In the reaction process, almost no residual TiB_2 remains in the FGM. Through the sintering process, the powders adhere together and the Ti–TiB FGM or monolithic plate is the final product. This process can be used to construct monolithic composites of constant volume fraction or composites graded along given dimensions. The change in composition of the constituents along a dimension is discrete and not truly continuous, although the distance over which a discrete change occurs can be very small and can closely approximate a continuous function over a larger distance. The FGM plates used in testing were graded over seven discrete layers of equal thickness with compositions ranging from 15% Ti–85% TiB to 100% Ti–0% TiB (see Table 2 for more precise details presented later in this article).

Ti–TiB composites are not new materials; in fact, the crystal structure of TiB was characterized by Decker and Kasper [21] as early as 1954. An extensive study of the microstructure and phases in Ti–TiB metal-matrix composites produced by reaction sintering was conducted by Sahay et al. [22] in 1999. The authors found that, at low volume fractions of TiB (up to $V^f = 0.30$), TiB whiskers are long, needle shaped, and randomly dispersed throughout the Ti matrix. At medium to high volume fractions of TiB (up to $V^f = 0.86$), colonies of densely packed TiB whiskers formed. At very high volume fractions of TiB ($V^f > 0.86$), the TiB formed a very coarse, elongated structure with very few whiskers present. In general, small traces of residual TiB_2 were detected in samples as the volume fraction of TiB increased. The fact that TiB reinforcement is produced in situ by chemical reaction makes the direct measurement of the basic material properties of TiB difficult, although Atri et al. [23] and Panda and Ravichandran [24] have had some success using methods rooted in crystal physics and experimentation. Recent technological advances have made the construction of such composites easier to accomplish; thus, their availability to academia and industry has grown [25,26].

The *key objectives* of this study are to 1) design and conduct impact experiments on metal–ceramic FGM plates to collect strain histories from the plates over the duration of the impact event, 2) construct a finite element simulation of the impact experiment that can be easily replicated by scientists and engineers in practice, and 3) correlate the results from the experiments and finite element models and draw conclusions regarding the validity of analytical and computational techniques used to study the response of FGM plate structures.

This article is organized as follows. An experimental technique for obtaining strain histories in plates subjected to impact loading will be presented, and the results of a series of impact tests with monolithic and functionally graded Ti–TiB composites will be discussed. Next, the details associated with a finite element model of the plate impact experiments developed to compare numerical simulations with the actual test data are presented. The finite element model incorporates two classes of material models. The first material model randomly distributes cells of Ti and TiB relative to local volume ratios. The second material model homogenizes material properties locally according to an analytical function of the volume fractions of the constituents. Each impact test was simulated using the finite element model, and the solutions from the computational model are compared with the experimental results, namely, with respect to historical trends, maximum strain magnitudes, and strain-rate effects. The article concludes with a discussion of the impact response of the graded plates in testing and simulation, as well as of the effective modeling of FGMs in engineering practice. The *key contribution* of this work is the validation of FGM material models and a computational framework for studying the impact response of FGM plates as a foundation for investigations of more severe impact loads at higher velocities and energy levels.

II. Plate Impact Experiments

The first objective of this work was to design and conduct impact experiments on metal–ceramic FGM plates to collect strain histories from the plates over the duration of the impact event. A series of impact experiments were conducted using monolithic Ti and Ti–TiB plates along with seven-layer Ti–TiB FGM plates. The strain histories give insight to the dynamic behavior of the physical specimens under these conditions that can be later compared with the numerical simulation.

A. Test Setup and Hardware

The plate specimens used in the tests were 7.62×7.62 cm^2 and 1.27 cm thick; there were ten plates in all. Six of the plates were monolithic in composition: two plates consisted of the American Society for Testing and Materials grade 2 commercially pure titanium; two plates consisted of 85% Ti–15% TiB; two plates consisted of 15% Ti–85% TiB. The remaining four plates were seven-layer Ti–TiB FGM. Each plate was instrumented with three 350 Ω large deformation strain gauges as shown in Fig. 1. The gauges were configured such that the bulk wires to the gauges were soldered to a terminal separate from the strain gauge and single-stranded jumper wires were then soldered to the actual gauge pads. This configuration is commonly used for dynamic tests in which inertial effects require minimizing the mass of the adhesive, strain gauge, and wiring assembly.

The Dynatup apparatus (developed by General Research Corp.), operated by the Air Vehicles Directorate (AFRL/RB) of the U.S. Air Force Research Laboratory at Wright–Patterson Air Force Base, was chosen to deliver impacts to the specimens at various velocities and energy levels. The Dynatup is shown in Fig. 2. The apparatus is designed to deliver impact energies up to 442 J to a specimen by converting a prescribed potential energy into kinetic energy. The Dynatup can supply a gravity-driven vertical impact of variable energy to a specimen in which the energy is controlled by the height of the load cell above the specimen and the mass attached to the crosshead assembly. Pneumatic spring assists can be used to provide further potential energy to the system to induce higher impact velocities and energy levels (this feature was not used in this study). A 2.54-cm-diam tup was used to transfer the dynamic loads to each specimen. The tup is composed of hardened steel and is cylindrical in shape with a hemispherical tip. The speed of the tup at impact is measured by a velocity photodetector wired into the Dynatup data

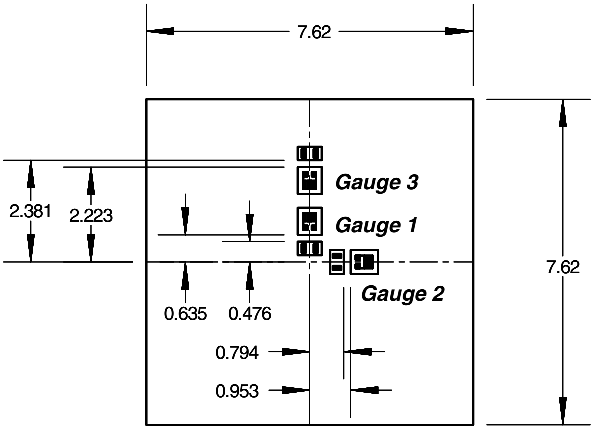

Fig. 1 Specification for specimen plates and strain gauge locations. All dimensions are in centimeters unless otherwise specified. The gauges are mounted on the bottom surface of the plate (titanium surface on layer 7 on FGM). Each plate is 1.27 cm thick, and the strain gauges are 0.318 cm wide and 0.635 cm long.

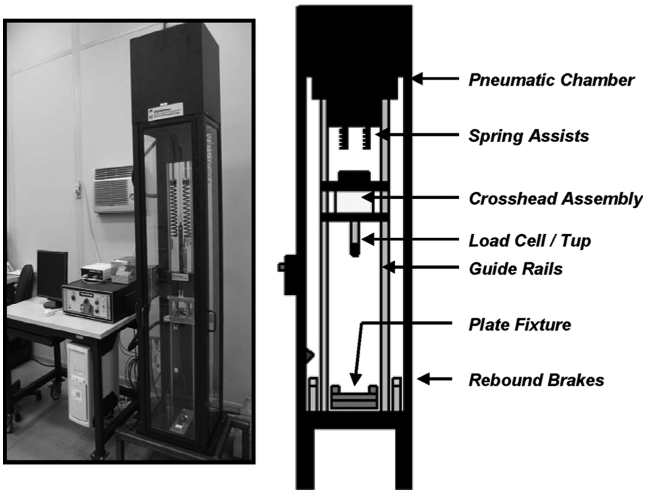

Fig. 2 Dynatup apparatus and accompanying schematic.

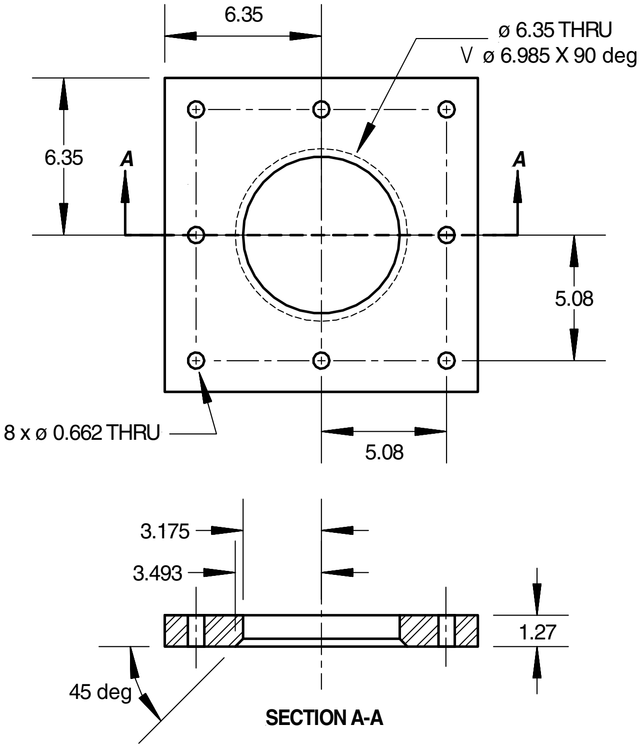

Fig. 4 Specification for the top plate of the specimen fixture. All dimensions are in centimeters unless otherwise specified. The top plate is machined from 304 stainless steel.

acquisition system. A set of pneumatic rebound brakes prevent a secondary impact from a rebound of the tup and crosshead.

A special fixture was constructed to hold the plate specimens for each test. Schematics of the fixture are shown in Figs. 3–6. The fixture was specifically designed to configure the plate specimens to behave as close to a plate with a circular boundary condition as possible. The fixture consists of a bottom plate with a circular opening that rests on the base of the Dynatup, a spacer plate that serves to position the square plates properly in the fixture while additionally preventing crushing of the plate during installation, and a top plate with a circular opening. The specimen plates are placed in the fixture such that the strain gauges lie on the (bottom) surface opposite the impact (top) surface. The components of the fixture were machined from 1.27-cm-thick 304 grade stainless steel. The three components are fastened together with eight (American) 1/4–28 unified course threads (UNF) screws (these will be referred to as the "fixture screws" from this point forward). The holes for the screws were tapped on the bottom plate such that the screws could be threaded into this component. The fixture assembly then attaches to the Dynatup with four 3/8–16 unified fine threads (UNC) screws (these will be referred to as the "Dynatup screws" from this point forward). The base of the Dynatup has tapped holes that the screws can be threaded into. The fixture screws were each torqued to 20 N · m, and the Dynatup screws were torqued to 35 N · m. These values were determined to simultaneously 1) prevent crushing of the Ti–TiB composites, 2) prevent separation of the fixture assembly components during impact, and 3) ensure the fixture assembly was secured in the Dynatup. The fixture and Dynatup screws are 18/8 grade stainless steel, a broader category of stainless steel that includes the 304 grade used for the fixture components. Figure 7 shows an FGM plate in the test fixture as installed in the Dynatup apparatus.

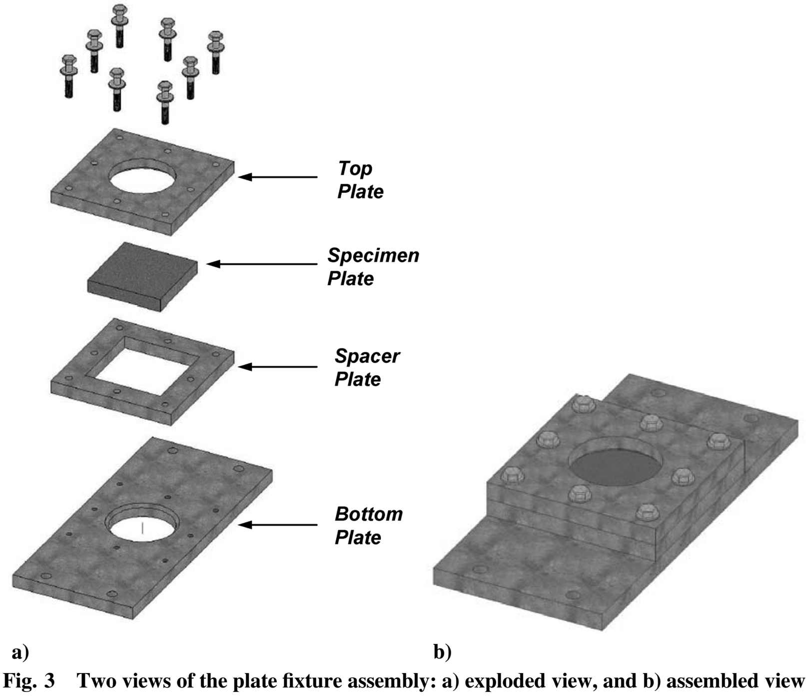

Fig. 3 Two views of the plate fixture assembly: a) exploded view, and b) assembled view.

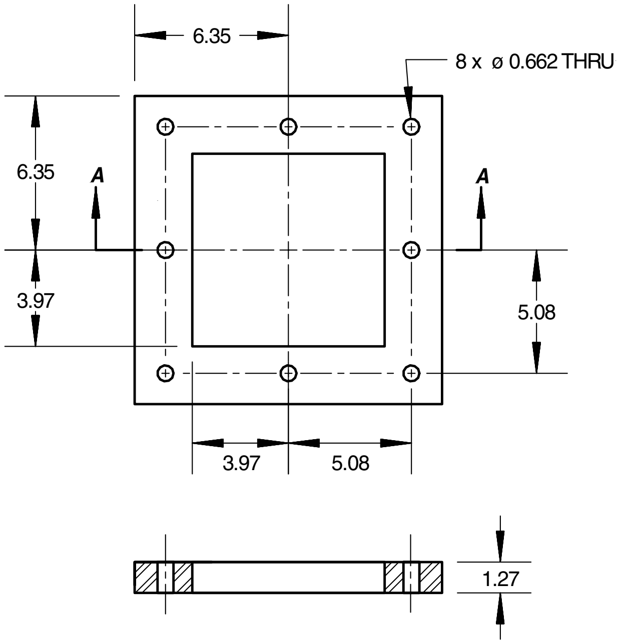

SECTION A-A

Fig. 5 Specification for the spacer plate of the specimen fixture. All dimensions are in centimeters unless otherwise specified. The spacer plate is machined from 304 stainless steel.

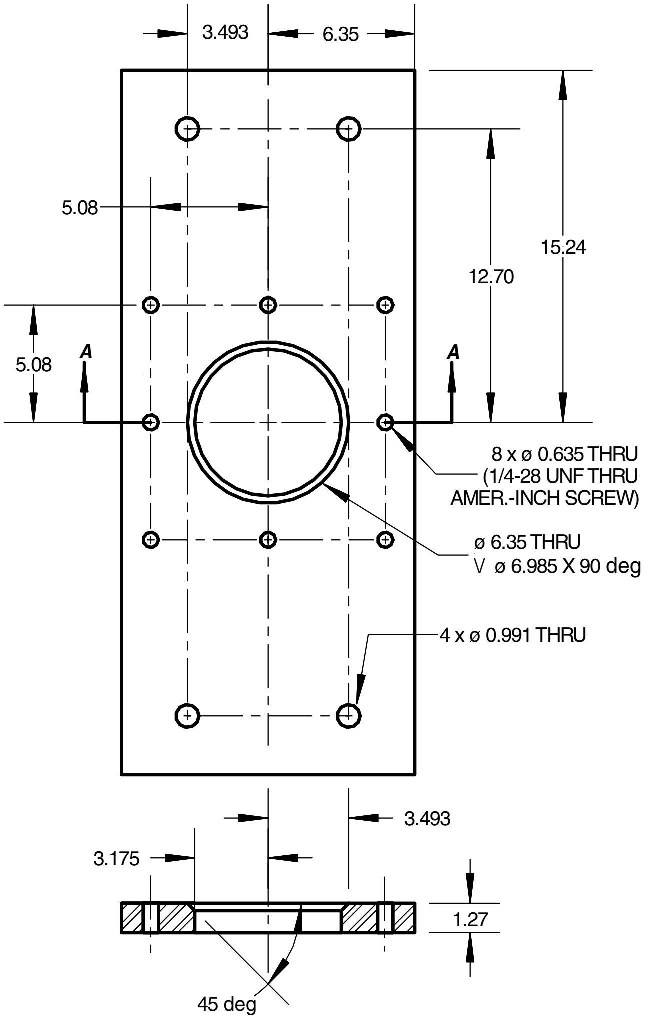

SECTION A-A

Fig. 6 Specification for the bottom plate of the specimen fixture. All dimensions are in centimeters unless otherwise specified. The bottom plate is machined from 304 stainless steel.

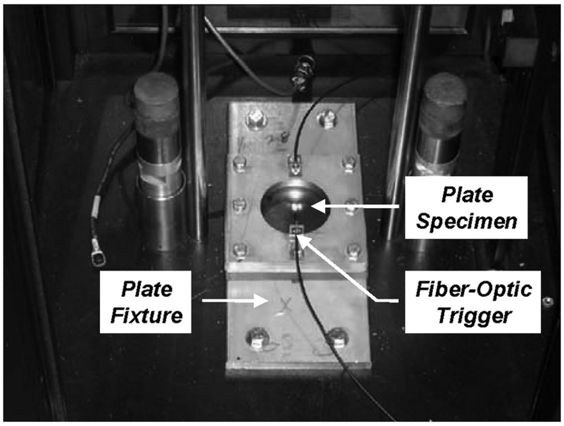

Fig. 7 Plate fixture with FGM plate installed in the Dynatup apparatus. Note the guide rails and rebound brakes from the Dynatup on either side of the fixture, as well as the fiber-optic sensor resting on the top plate.

Once the plate and fixture assembly were installed in the Dyantup, the strain gauges were wired into a signal conditioning system using a standard 1/4 Wheatstone bridge arrangement with 5.0 V of excitation. The conditioner uses dc differential amplifiers with 80 kHz of bandwidth. The output from the signal conditioners/amplifiers was input to an oscilloscope programmed to collect 10,000 samples over a 2000 μs window. A fiber-optic sensor was used to automatically trigger data collection from the oscilloscope. The sensor, composed of a transmitter, receiver, and amplifier, emits a light beam that sends a voltage signal to the oscilloscope when the beam is interrupted. A single sensor was placed directly above the impact site on each specimen, and the beam was interrupted as the tup passed through the beam just before contact with the plate. By triggering data collection in this fashion, the strain histories from the impact event were wholly captured without interference or premature triggering of the system due to background noise. The next section outlines the procedure by which the strain histories were collected.

B. Test Procedure

The test procedure for collecting strain histories is summarized as follows:

1) The specimen is fitted with strain gauges as shown in Fig. 1 on the bottom surface of the plate. The surface of the plate with the gauges will be the surface opposite the impact surface.

2) The plate is installed and centered into the test fixture and each of the fixture screws is torqued to 20 N · m.

3) The specimen/fixture assembly is placed in the Dynatup and the Dynatup screws are torqued to 35 N · m.

4) The Dynatup crosshead is raised above the impact surface of the plate to a prescribed height (see Table 1). The height is measured from the tip of the tup to the impact surface of the plate.

5) The fiber-optic sensor is armed; the oscilloscope and signal conditioner are prepared for data acquisition.

6) The Dynatup system is armed to release the crosshead for impact against the specimen plates.

7) The crosshead is released; the potential energy stored in crosshead assembly is converted into kinetic energy.

8) A velocity photodetector records the speed of the tup at impact; the tup impacts the top surface of the plate.

9) The local and global deformation of the plate are recorded through the strain histories collected by the three strain gauges attached to the bottom surface of the plate during the entire impact event.

10) The rebound brakes in the Dynatup engage and prevent the tup from multiple impacts due to rebound.

11) The strain history is recorded and the test is completed.

C. Test Results

Ten specimens were tested using only gravity-driven impacts with the Dynatup. The speed of the tup just before impact was recorded,

Table 1 List of plate impact experiments

Test no.	Plate specimen	Crosshead mass, kg	Crosshead height, m	Ideal impact velocity, m/s	Actual impact velocity, m/s	Impact energy, J
1	100% Ti, 0% TiB monolithic	13.06	0.508	3.157	3.040	60.35
2	100% Ti, 0% TiB monolithic	13.06	0.635	3.530	3.476	78.90
3	85% Ti, 15% TiB monolithic	13.06	0.508	3.157	3.050	60.75
4	85% Ti, 15% TiB monolithic	13.06	0.635	3.530	3.479	79.04
5	15% Ti, 85% TiB monolithic	13.06	0.381	2.734	2.585	43.63
6	15% Ti, 85% TiB monolithic	13.06	0.508	3.157	3.050	60.75
7	Seven-layer Ti–TiB FGM	13.06	0.508	3.157	3.040	60.35
8	Seven-layer Ti–TiB FGM	13.06	0.635	3.530	3.412	76.02
9	Seven-layer Ti–TiB FGM	13.06	0.762	3.867	3.765	92.56
10	Seven-layer Ti–TiB FGM	13.06	0.889	4.176	4.078	108.6

and the impact energy associated with the velocity was tabulated. One column of Table 1 shows the ideal impact velocity given the initial height above the plate specimen and the mass of the crosshead assembly. The ideal impact velocity assumes that, upon release of the crosshead from rest, all potential energy stored in the crosshead is converted to kinetic energy on impact with no work performed on the system or losses from external sources:

$$\mathrm{KE}_1 + \mathrm{PE}_1 + W_{1\to 2} = \mathrm{KE}_2 + \mathrm{PE}_2 \tag{1}$$

$$\tfrac{1}{2}mv_1^2 + mgh_1 + W_{1\to 2} = \tfrac{1}{2}mv_2^2 + mgh_2 \tag{2}$$

where KE and PE are the kinetic and potential energy of the crosshead assembly in states 1 and 2, illustrated in Fig. 8. $W_{1\to 2}$ is the external work (*or losses in the system*) performed from state 1 to state 2. In the ideal scenario, $W_{1\to 2}$ is zero; in the actual tests, losses due to friction or other external sources are included in this term and $W_{1\to 2}$ is negative (indicating a loss). In Eq. (2), m is the mass of the assembly, h is the height measured from the tip of the tup to the top surface of the specimen plate, v is the velocity of the crosshead assembly, and g is the gravitational constant. It is clear from the data that there are indeed losses in the system. These losses could be attributed to any or multiple factors including friction, vibration in the guide rails, drag, and uneven motion of the crosshead during a drop test.

Strain histories were successfully collected from eight of the ten tests. The tests involving the 15% Ti–85% TiB monolithic samples (tests 5 and 6) were the two unsuccessful tests. These specimens fractured severely immediately after impact and virtually no data was collected on these specimens as a result. The FGM specimen from test 10 also fractured; however, a significant portion of the strain history was collected before failure and this history has been included.

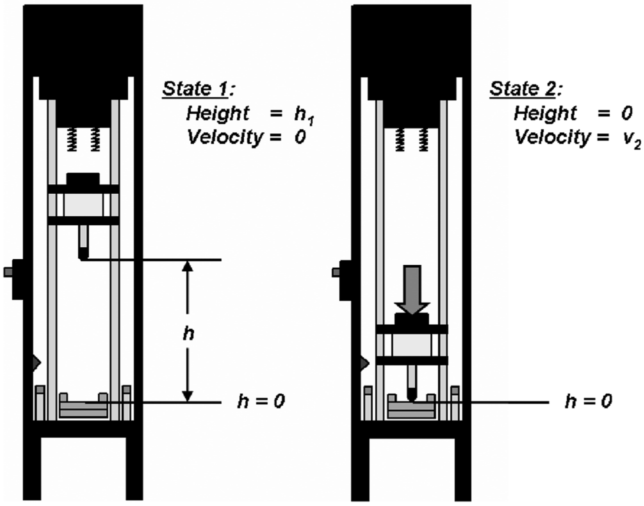

Fig. 8 Illustration of kinetic, potential energy states in the Dynatup apparatus for the given impact test.

Tests 5 and 6 were unsuccessful, as noted earlier, and these tests are not included. For brevity, only the strain histories from gauges 2 and 3 (see Fig. 1) are shown. Note that gauges 1 and 2 were close in radial proximity and the data from these gauges are only slightly different in magnitude. The results from gauges 2 and 3, reading strains in perpendicular directions and themselves not as close in radial proximity, provide better results for discussion. Significant outliers were removed from the histories and these data were smoothed using the well-known robust locally weighted regression (or *loess*) technique developed by Cleveland [27] and Cleveland and Devlin [28] with a quadratic polynomial regression and weighted least squares over a range of 40 data points. The choice of weighted least-squares over 40 data points is large enough that significant oscillations in the plates are not lost while simultaneously ensuring that the noise present in the signals is eliminated. The reader will also note that in a few areas there are gaps in the strain histories. This is due to the removal of outliers from electrical shorts in the gauges that occurred during the impact event and history collection. The results from the tests will be discussed more extensively in Sec. IV in which they are compared with the results from the finite element models.

III. Finite Element Models

The second objective of this work was to construct a finite element simulation of the impact experiment that could be easily replicated by scientists and engineers in practice. Finite element models (FEMs) of the plate impact experiments were thus designed to numerically simulate the tests. In this section, information pertinent to the development of the models is presented. The commercial code ABAQUS [29] was used to simulate the tests. The simulations covered the 2000 μs window of the event. Explicit integration was used to solve the governing equations to take full advantage of the computational efficiency and the inherent effectiveness at solving dynamic, wave-oriented models. One thousand data points of strain were recovered from the solution database. Strain data were collected only from nodes directly under each strain gauge grid, and only strain outputs oriented along the principal direction of the strain gauges were used to compare with the experimental strain histories. This is an important point to remember because the state of strain is a complex three-dimensional state at virtually all points in the plate during the impact event, and the strain gauge measures only the component of strain (directly) along the principal direction of the gauge. The following paragraphs outline specific details associated with the material models, geometries and meshes of the components, loads, constraints, boundary conditions, and contact interactions.

A. Material Models

Two material models were used to simulate material properties in this work: 1) the two-phase material model, and 2) the homogenized-layers material model. Before discussing the material models, the properties for titanium and titanium boride will be assumed for the remainder of this paper. The material properties for commercially pure titanium [30] are 1) elastic modulus, $E = 110$ GPa; 2) Poisson's

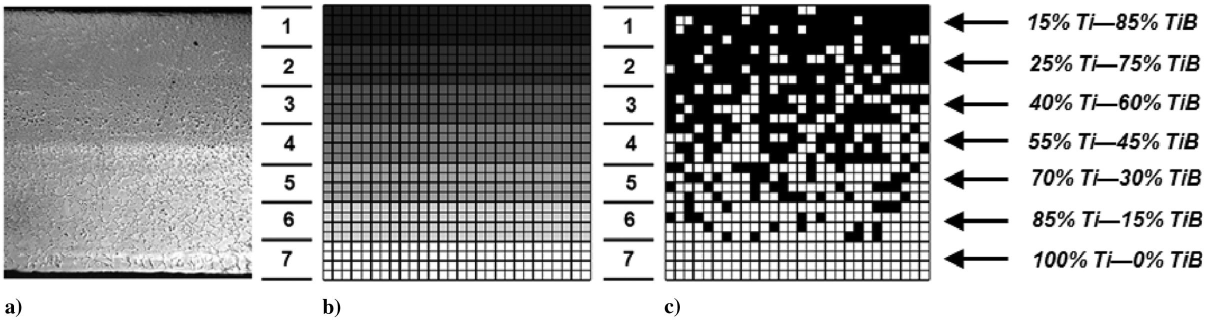

Fig. 9 Cross sections of the seven-layer BAE Systems Ti–TiB FGM: a) the actual FGM, b) the two-phase model, and c) the homogenized-layers model. Black cells represent TiB-only elements; white cells represent Ti-only elements. The homogenized layers are shaded based on the volume ratio of Ti to TiB.

ratio $= 0.340$; and 3) density, $\rho = 4510\ \mathrm{kg/m^3}$. The material properties for titanium boride (provided via correspondence with BAE Systems) are 1) elastic modulus, $E = 370$ GPa; 2) Poisson's ratio $= 0.140$; and 3) density, $\rho = 4630\ \mathrm{kg/m^3}$.

The two-phase material model randomly distributes metal and ceramic-only cells (i.e., elements) constrained by the local volume fraction of the constituents. In the case of the Ti–TiB FGM system, each cell (or element) contains the material properties of only titanium or only titanium boride. Suppose that a layer of FGM plate contains 100 elements and consists of 70% Ti and 30% TiB. Using the two-phase material model, 70 elements would be titanium and 30 elements would be titanium boride in that layer. This model allows the random nature of the particulate distribution to be considered, which can be important to understanding how local distributions of constituents contribute to local effects such as wave propagation, plasticity, and damage (these effects are not studied in this article). The size and geometry of each cell is very important to the analysis and can ultimately affect the results. An illustration of the two-phase model is shown in Fig. 9.

The homogenized-layers material model uses analytical equations relating the material properties of the constituents and the volume fractions of the constituents to the net material properties of the composite. There are many such analytical functions that have been developed over the years. These functions vary in complexity from relatively simple relations such as the classical rule of mixtures [31], to the self-consistent model [32–34] based on more rigorous physics and mathematics, to those that account for statistical distributions of constituents and their geometries at the micromechanical level [35]. The advantage of using these functions is that definite quantitative properties can be obtained for well-defined regions of constant volume fraction ratio, thus eliminating the need for extensive knowledge of the microstructure. These models are typically used when formulating the analytical behavior of FGM structures using principles of continuum mechanics.

The chosen analytical relations for homogenizing local material properties in the monolithic and functionally graded composites are the Mori–Tanaka estimates. Mori and Tanaka [36] demonstrated that, in two-phase composites, that is, a matrix with randomly distributed misfitting inclusions, the average internal stress in the matrix is uniform throughout the material and independent of the position of the domain in which the average is obtained. They also showed that the actual stress in the matrix is the average stress in the composite plus a locally varying stress, the average of which is zero in the matrix phase. Benveniste [37] used their analysis as the basis for developing equations that can be used to determine bulk and shear moduli for the composite material as a whole:

$$\frac{K-K_1}{K_2-K_1} = \frac{V_2^f C_1}{(1-V_2^f)+V_2^f C_1}; \qquad \frac{G-G_1}{G_2-G_1} = \frac{V_2^f C_2}{(1-V_2^f)+V_2^f C_2} \tag{3}$$

The subscripts 1 and 2 represent the individual constituents, whereas no subscript on K and G indicate the bulk and shear moduli for the composite. V^f is the volume fraction of a given constituent. The expressions in Eq. (3) are explicit, and the variables C_1 and C_2 depend on the nature of the particle inclusions. Berryman [38,39] developed a framework for the two special cases of needle and spherical inclusions. The special case of needle inclusions will be the focus, as the TiB in the monolithic and graded composites is primarily in a whisker/needle morphology. The constants C_1 and C_2 are given as follows:

$$C_1 = \frac{K_1 + G_1 + (1/3)G_2}{K_2 + G_1 + (1/3)G_2} \tag{4}$$

$$C_2 = \frac{1}{5}\left(\frac{4G_1}{G_1+G_2} + 2\frac{G_1+f_1'}{G_2+f_1'} + \frac{K_2+(4/3)G_1}{K_2+G_1+(1/3)G_2}\right) \tag{5}$$

$$f_1' = \frac{G_1(3K_1+G_1)}{(3K_1+7G_1)} \tag{6}$$

The elastic properties E and v for each composite layer of Ti–TiB can be solved for by taking the results from Eq. (3) in each layer and relating those results to the definitions of bulk and shear moduli in terms of these properties:

$$K = \frac{E}{3(1-2\nu)}; \qquad G = \frac{E}{2(1+\nu)} \tag{7}$$

The Mori–Tanaka needle (MTN) estimates do not account for material density, a necessary material property in dynamic analyses. The density ρ of each composite layer is usually determined using the classical rule of mixtures, and Eq. (8) shows the relation that was used to find this property in individual layers:

$$\rho = V_1^f \rho_1 + V_2^f \rho_2 \tag{8}$$

Table 2 shows the effective material properties for each layer in the functionally graded plates using the MTN estimates and the rule of mixtures for density. An illustration of the homogenized-layers model compared with the two-phase model and an actual Ti–TiB FGM plate is shown in Fig. 9.

B. Model Components

The FEM of the test can be effectively divided into the following components: 1) the specimen plate fixture with its bottom, spacer, and top plates; 2) the eight fixture screws; 3) the four Dynatup screws; 4) the idealized tup; and 5) the specimen plate. The complete FEM mesh is shown in Fig. 10. The entire model was meshed with linear, eight-noded, three-dimensional solid continuum brick elements. Linear bricks of this type were chosen primarily for computational efficiency.

The top, bottom, and spacer plate components of the fixture were machined from 304 stainless steel, as mentioned in the previous section. The parts were manually constructed and meshed in ABAQUS according to the specifications shown in Figs. 4–6. This

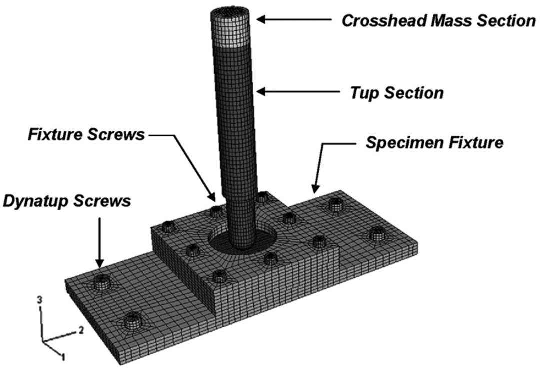

Fig. 10 Finite element model of plate impact experiments.

was done to maintain a consistent mesh and prevent the formation of irregularly shaped elements that could potentially cause numerical problems during solution. The bottom plate consists of 7935 nodes and 5656 elements, the spacer plate consists of 3800 nodes and 2560 elements, and the top plate consists of 4280 nodes and 2944 elements. The actual fixture components were visually inspected after testing and found to be virtually undeformed. The components are thus assumed to require only elastic material properties. The material properties used in the FEM for 304 grade stainless steel [30] are 1) elastic modulus, $E = 193$ GPa; 2) Poisson's ratio $= 0.290$; and 3) density, $\rho = 8030\ \mathrm{kg/m^3}$.

The eight fixture screws are American 1/4–28 UNF composed of 18/8 grade stainless steel (note that 18/8 stainless steel is a broad category of stainless steel alloys containing 18% chromium and 8% nickel; 304 stainless steel alloy is a member of this category). The geometry of the screws was simplified in the finite element model. Each hex screw's head is nominally 0.397 cm thick, and the width across the flats is 1.111 cm [30]. Round washers used in conjunction with the screws were also 18/8 stainless steel and were nominally 0.198 cm thick with an outside diameter slightly larger than the width across the flats of the head. The simplified finite element model consists of a round cylinder for the head with a diameter equal to the width across the flats of the hex-head screw and a thickness equal to the hex head plus the washer thickness (thus effectively combining the washer and head into one geometry). The stud length is equal to the thickness of all three fixture plates sandwiched together (3.81 cm), and the diameter of the stud is 0.635 cm. Each of the eight fixture screws contains 1300 nodes and 1040 elements; the total number of nodes and elements contained in the fixture screws are, thus, 10,400 and 8320, respectively. The four Dynatup attachment screws are American 3/8–16 UNC and are also composed of 18/8 grade stainless steel. Each hex screw's head is 0.595 cm thick, and the width across the flats is 1.429 cm [30]. The round washers used in conjunction with the screws were the same 18/8 stainless steel as the screws and were 0.198 cm thick with an outside diameter slightly larger than the width across the flats of the hex head. The simplified finite element model consists of a round cylinder for the head with a diameter equal to the width across the flats of the hex-head screw and a thickness equal to the hex head plus the washer thickness. The stud length is equal to the thickness of the bottom plate (1.27 cm), and the diameter of the stud is 0.953 cm. Each of the four Dynatup screws contains 641 nodes and 480 elements; the total number of nodes and elements for these components is thus 2564 and 1920, respectively. The same screws were used in all impact tests and were virtually undeformed after testing; therefore, only elastic properties were input into the finite element models. The same properties used for 304 stainless steel were used for 18/8 stainless steel.

The crosshead, load cell, and tup assembly in the Dynatup apparatus represent a very unique part of the FEM as a whole. The best scenario for modeling the Dynatup apparatus is to include nearly all the parts that make up the assembly, which is itself not a trivial matter. The primary function of the crosshead, load cell, and tup assembly is to transfer energy and momentum to the target specimen through contact between the tup and specimen. A highly simplified model of this assembly was developed that would serve both of these purposes (referred to as simply the "tup FEM" or "tup model" from this point forward). It consists of two unique sections: 1) a tup section, and 2) a crosshead-mass section. The tup section is composed of two cylindrical pieces; one piece is 3.175 cm in diameter and 13.97 cm long, and one piece is 2.54 cm in diameter and 4.445 cm long. At the end of the smaller cylinder is a hemispherical tip of radius 1.27 cm. The larger cylinder represents the load cell, and the smaller cylinder with hemispherical tip is the tup. The net length of this section is, thus, 19.69 cm. The crosshead-mass section is a cylinder 2.54 cm long and 3.175 cm in diameter. The net length of the entire tup model is, thus, 22.23 cm. The actual composition of the load cell and tup was not known and not provided for proprietary reasons. A set of material properties thus had to be assumed for the tup section, and 4340 hardened-alloy steel was chosen. Material properties for this steel alloy [30] are 1) elastic modulus, $E = 200$ GPa; 2) Poisson's ratio $= 0.290$; and 3) density, $\rho = 7800\ \mathrm{kg/m^3}$. The total mass of the tup section, given the density of 4340 hardened-alloy steel, was 1.072 kg. The crosshead-mass section was designated as a pseudomaterial; the purpose of this section was to store the remainder of the entire mass of the crosshead-load cell-tup assembly without constructing the entire crosshead. From Table 1, the mass of the entire assembly during testing was 13.06 kg. Knowing the dimensions of the crosshead-mass section in the FEM, this remaining mass (11.99 kg) was distributed through this small volume and incorporated in the model by applying a calculated density to the elements of that section. Also noteworthy is the fact that the elastic modulus was set very high in comparison with the rest of the model components; essentially the crosshead-mass section behaves like an rigid mass attached to a deformable load cell tup. Material properties for this pseudomaterial are 1) elastic modulus, $E =$ infinity GPa (i.e., a very large discrete number that ABAQUS can process); 2) Poisson's ratio $= 0.300$; and 3) density, $\rho = 596123\ \mathrm{kg/m^3}$. The tup model contains 12,190 nodes and 11,008 elements total.

Finally, the plate specimens were constructed as $7.62 \times 7.62\ \mathrm{cm^2}$ and 1.27 cm thick. A computer script was programmed to generate the mesh and assign material properties to individual elements in the plate model. For the two-phase model, the individual Ti and TiB elements are randomly distributed according to their local volume fraction ratios by the computer script using a random number generator algorithm. For the homogenized-layers model, the material properties for the elements in each layer are calculated by the same equations discussed earlier and assigned as such (see Table 2). A

Table 2 Homogenized-material properties within FGM layers

			Mori–Tanaka needle estimate		
Layer	Volume Ti, %	Volume TiB, %	Elastic modulus, GPa	Poisson ratio	Density, $\mathrm{kg/m^3}$
1	15	85	315.0	0.175	4612
2	25	75	282.7	0.196	4600
3	40	60	239.4	0.227	4582
4	55	45	201.4	0.256	4564
5	70	30	167.6	0.284	4546
6	85	15	137.4	0.312	4528
7	100	0	110.0	0.340	4510

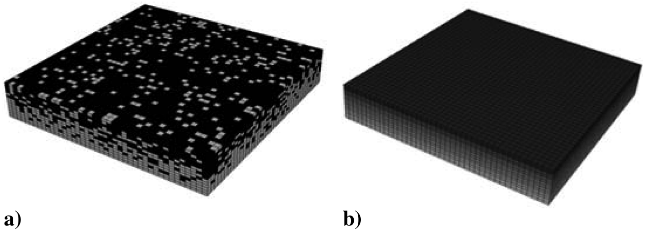
a) b)

Fig. 11 Comparison of the finite element representations of the FGM plates: a) the two-phase material model, and b) the homogenized-layers model. Black cells represent TiB-only elements; white cells represent Ti-only elements. The homogenized layers are shaded based on the volume ratio of Ti to TiB.

study was undertaken to determine the mesh that would be most effective from both a computational and solution convergence standpoint. The plate mesh used here, based on the study, was 14 elements through the thickness of the plate and 42 element divisions along each side of the plate; thus, the total number of nodes and elements for the plates were 27,735 and 24,696, respectively. Increased mesh density for the plates showed virtually no improvement in the FEM solutions while significantly increasing computational expense. Material properties were assigned based on the use of the two-phase or homogenized-layers model discussed earlier. Figure 11 shows a sample of the specimen plate using each model.

C. Boundary Conditions, Constraints, and Loads

The following boundary conditions and constraints were applied to the model. Note the orientation of the coordinate axes in Fig. 10 when reading this paragraph.

1) The bottom surface of the bottom plate was constrained from vertical displacement only (direction 3). This surface is in direct contact with the base of the Dynatup. The Dynatup base is made of 5.08 cm steel and is not easily deformable; thus, this assumption was deemed prudent.

2) An imaginary plane parallel to the 1–3 plane passing through the center of the fixture assembly was constrained such that all nodes and element faces contained directly in this plane were not allowed translations parallel to the 2-axis direction. This included the bottom, spacer, and top plates of the fixture as well as the specimen plate; nodes or elements attached to the tup and plate fastener screws were not assigned this restriction.

3) An imaginary plane parallel to the 2–3 plane passing through the center of the fixture assembly was constrained such that all nodes and element faces contained directly in this plane were not allowed translations parallel to the 1-axis direction. This included the bottom, spacer, and top plates of the fixture as well as the specimen plate; nodes or elements attached to the tup and plate fastener screws were not assigned this restriction.

4) The four Dynatup attachment screws were threaded into the Dynatup base. The FEM stud length of these screws was shortened to a length equal to the thickness of the bottom plate of the fixture (1.27 cm). Once threaded and torqued to the required level, it is assumed that the screws could not be pulled out of the Dynatup base. Thus, the bottom surface of each Dynatup screw (that is, the surface contained in the same plane as the Dynatup base-fixture bottom plate interface) was constrained from vertical deflection only.

5) The axes of the four Dynatup attachment screws were constrained from motion in the 1 and 2 directions.

6) The axis of the tup was constrained from motion in the 1 and 2 directions.

7) Recall that the fixture screws were threaded into the bottom plate only. The holes in the spacer and top plates were through-holes only. In the FEM, the holes in the bottom plate were made to be the same diameter as the stud diameter of the fixture screws; the holes in the other two plates were made slightly larger. Therefore, a small portion of the outside surfaces of the screws along the stud length will coincide with the surfaces inside the holes of the bottom plate throughout the thickness of the plate. To simulate a tight, rigid connection between the fixture screws and the threaded holes of the bottom plate, the nodes attached to the coincident surfaces of the bottom plate and the screws in each hole were constrained to have identical displacements in all three principal directions. This constraint is assumed to model a threaded connection without requiring an actual model of the threads themselves.

ABAQUS has the capability of modeling contact interactions between various components of the model assembly. Contact in the realm of finite element theory is a highly nonlinear analysis and requires special treatment [40,41]. The contact law used exclusively in this finite element model was that of rigid-hard contact. The main feature of this law is that it is essentially an on–off law in which the pressure applied from one object to another is zero when the objects are not in contact and positive when in contact; the magnitude of pressure is a function of the interpenetration of the two object surfaces in contact. This contact law was applied to the following surfaces: 1) the interface of the bottom and spacer plates of the fixture, 2) the interface of the spacer and top plates of the fixture, 3) the interface of the specimen plate and the fixture bottom plate, 4) the interface of the specimen plate and the fixture top plate, 5) the top surface of the specimen plate and the surface near the tip of the tup, 6) the top surface of the fixture top plate and each surface underneath the head of each fixture screw, and 7) the top surface of the fixture bottom plate and each surface underneath the head of each Dynatup attachment screw.

In the actual plate impact experiments, the primary load to the plates was the impact load delivered by the tup. In the assembly of the FEM, the tup was placed above the specimen plate with 0.1 mm of separation initially between the two objects. A velocity field was applied to the entire tup model in the FEM as an initial condition with a magnitude equal to the speed measured during the test (see Table 1). Incidentally, the velocity field has components in only the vertical 3 direction; thus, the speed and the magnitude of that component of the velocity field are identical. The tup maintains this speed until contact is established between the tup and the specimen plate. Once this occurs, the dynamics of the system take over and the instantaneous velocity of the tup must be determined based on the solution to the finite element model.

A note on the torque loads applied to the Dynatup and fixture screws is in order. Recall that each of the four Dynatup screws were torqued to a 35 $\mathrm{N \cdot m}$ load and the eight fixture screws were torqued to a 20 $\mathrm{N \cdot m}$ load. It was noticed that these torque loads did not appear to visually deform the fixture plates or the screws themselves during screw preloading or after impact tests occurred. A subsequent analysis of the force loading on the screws using analytical and finite element techniques verified the hypothesis that the deformation in the fixture plates and screws was negligible during preloading of the screws. For this reason, the torque loading on the screws was left out of the FEM. Further analysis showed that the deformation of the specimens during impact induced noticeable lifting forces and potential separation of the fixture plates from the specimen leveraging against the fixture. This action produced stresses in the fixture screws as they resist the leveraging and fixture plate separation. With the screws in direct contact with the fixture component plates and threading accounted for in the constraints of the system, it was deemed that this was sufficient to emulate the behavior of the fixture plate fastening.

IV. Results and Analysis

The third and final objective of this work was to correlate the results from the experiments and finite element models and draw conclusions regarding the validity of analytical and computational techniques used to study the response of FGM plate structures. In this section, the results from the experiments and finite element analyses are presented for direct comparison. The primary goals are to assess the validity of the material models (two phase vs homogenized layers) and determine whether FGMs can be effectively modeled and studied using finite element methods. Comparisons and analysis will be performed in three specific areas: 1) a qualitative comparison of the strain history plots from the experiments and FEM, 2) a quantitative assessment of the predicted maximum strains in the plates during the impact events, and 3) an investigation of the strain rates applied to the plates during each impact load.

A. Experiment Versus FEM Strain Histories

The strain histories from strain gauges 2 and 3 are plotted along with the results from the two-phase material model and the Mori–Tanaka homogenized-material model with needle inclusions. Strain data were collected only from nodes directly under each strain gauge grid, and only strain components oriented along the principal direction of the strain gauges were used to compare with the experimental strain histories. Figures 12–19 show the results from the FEMs next to the experimental data.

The titanium plates in tests 1 and 2 (Figs. 12 and 13) were modeled using only the two-phase material model. Note that the MTN estimates for the case of 100% Ti would simply return material properties and material distribution precisely the same as the two-phase material model; therefore, the two analyses are redundant. The histories predicted by the FEM match up extremely well with the test results. This is very important in that it validates the modeling of the FEM given the geometry, loading, and constraints on the model.

The histories from the 85% Ti–15% TiB monolithic plate tests (tests 3 and 4, Figs. 14 and 15) match well with the exception of the histories in test 3, gauge 2. The response in gauge 2 indicates that the impact event is occurring over a larger period than reflected in gauge 3, lending credence to the theory that the unloading of the gauges may be a source of the discrepancy between test and simulation. Here, the two-phase and homogenized-layers models were used in these FEMs and are plotted against the experimental histories. This was the next step in the FEM validation of the impact tests. These monolithic plates have a constant volume fraction ratio of Ti to TiB. The homogenized-layers model of this specimen is a plate composed of a single layer of constant material properties. The two-phase model is composed of a random distribution of Ti to TiB in which 85% of the elements in the plate are Ti and 15% of the elements in the plate are TiB. These tests and FEMs thus present an added level of complexity above the plate specimens composed of pure Ti and demonstrate that the material models and FEM are suitable for extension to modeling the more complex FGM plates.

Figures 16–19 show the histories for the FGM plates. Again, the FEM simulations match the strain histories reasonably well from a qualitative standpoint. Recall that the FGM plate in test 10 failed midway through the impact event. Given the degree of correlation to this point, it is reasonable to assume that the FEM simulates the data well and the predicted histories from the FEM indicate how the plate would behave had failure not occurred. Whether or not it is valid to

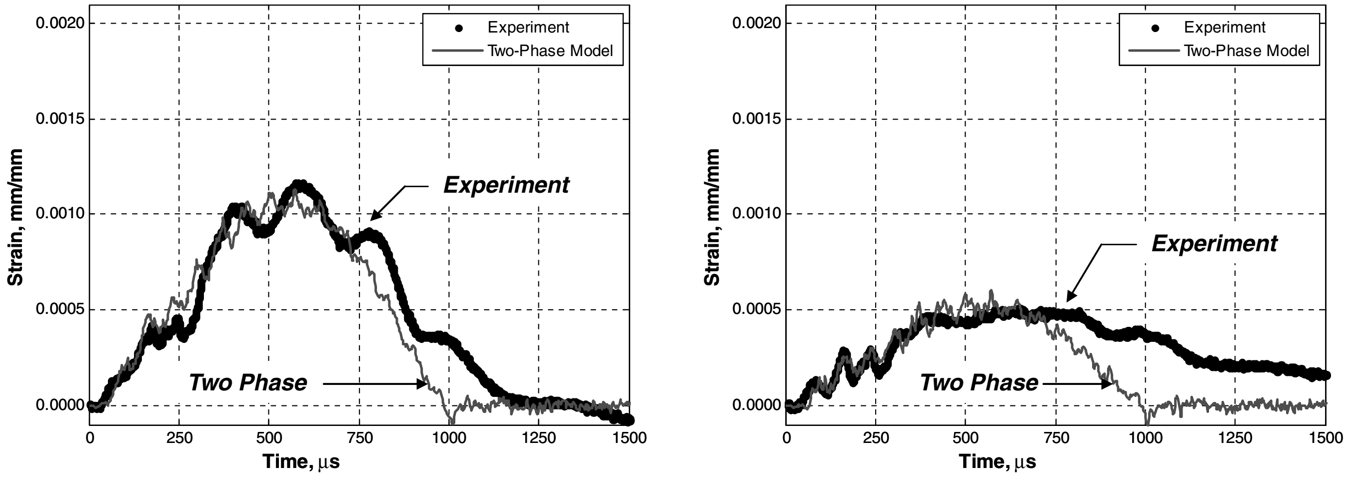

a) b)

Fig. 12 Test 1 strain histories vs FEM results: a) strain gauge 2, and b) strain gauge 3. Specimen was 100% Ti–0% TiB monolithic with an impact velocity of 3.040 m/s.

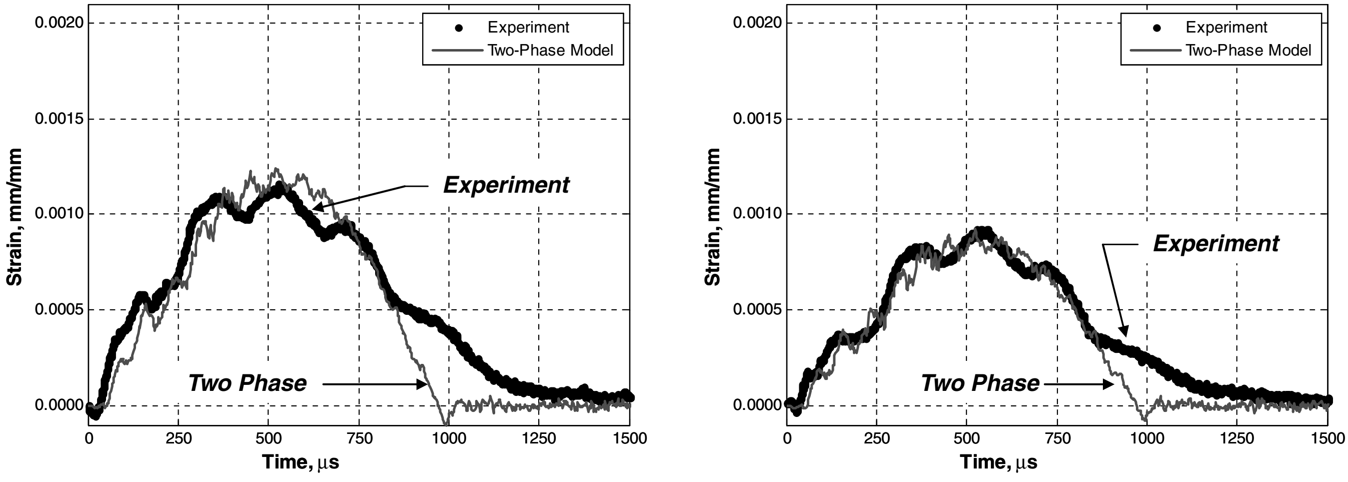

a) b)

Fig. 13 Test 2 strain histories vs FEM results: a) strain gauge 2, and b) strain gauge 3. Specimen was 100% Ti–0% TiB monolithic with an impact velocity of 3.476 m/s.

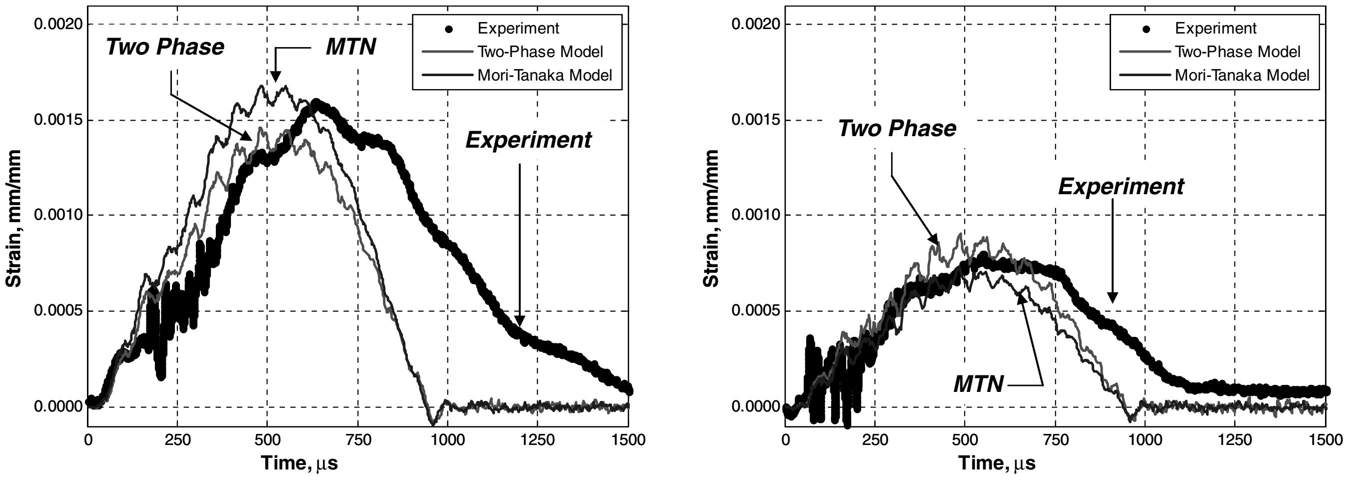

a) b)

Fig. 14 Test 3 strain histories vs FEM results: a) strain gauge 2, and b) strain gauge 3. Specimen was 85% Ti–15% TiB monolithic composite with an impact velocity of 3.050 m/s.

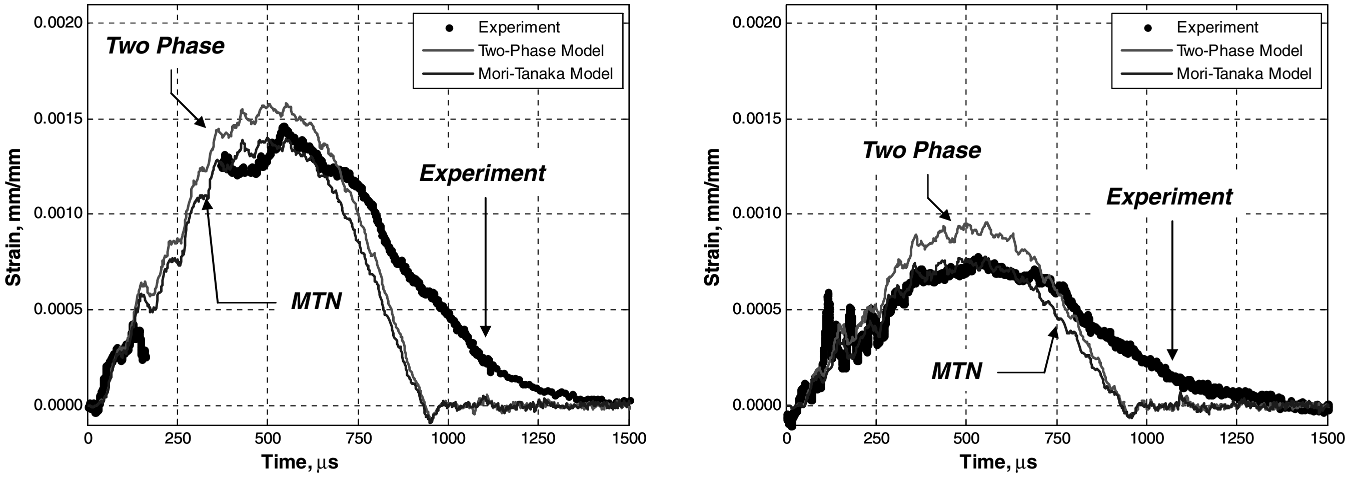

a) b)

Fig. 15 Test 4 strain histories vs FEM results: a) strain gauge 2, and b) strain gauge 3. Specimen was 85% Ti–15% TiB monolithic composite with an impact velocity of 3.479 m/s.

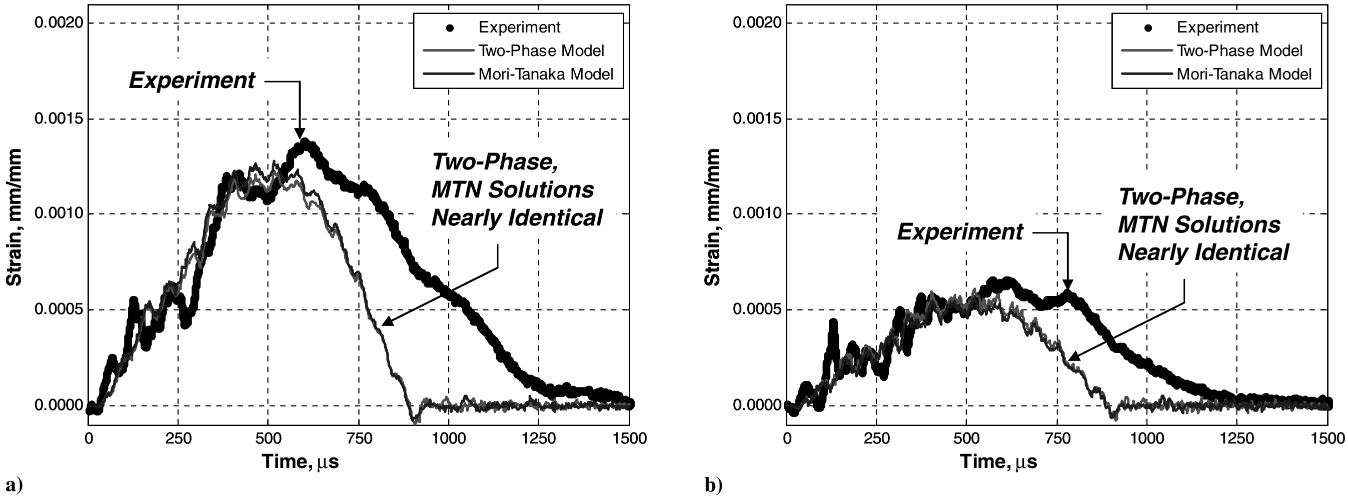

a) b)

Fig. 16 Test 7 strain histories vs FEM results: a) strain gauge 2, and b) strain gauge 3. Specimen was seven-layer FGM with an impact velocity of 3.040 m/s.

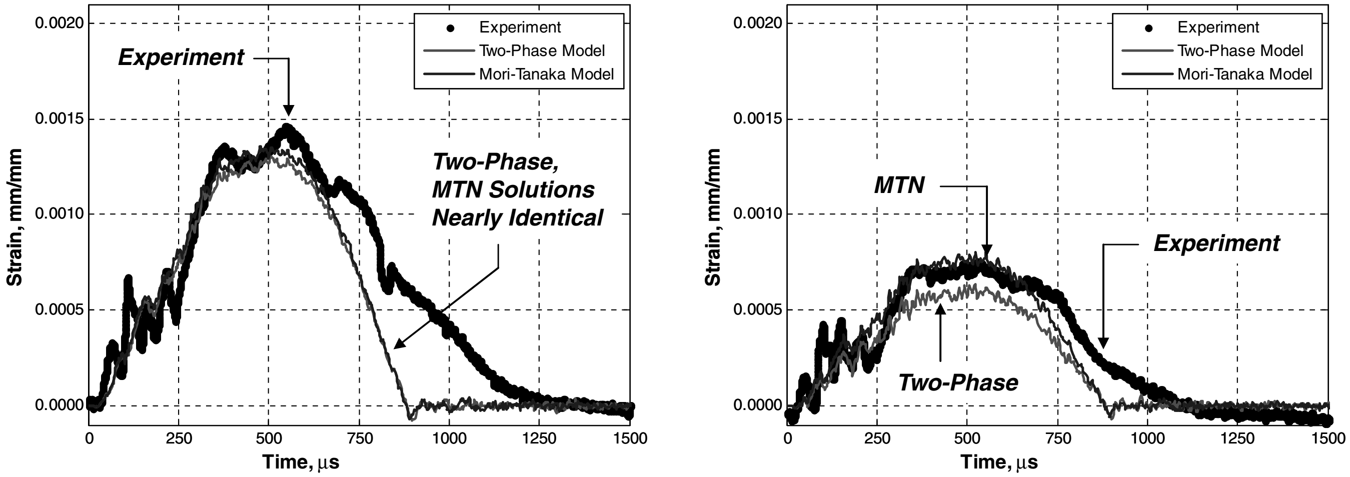

a) b)

Fig. 17 Test 8 strain histories vs FEM results: a) strain gauge 2, and b) strain gauge 3. Specimen was seven-layer FGM with an impact velocity of 3.412 m/s.

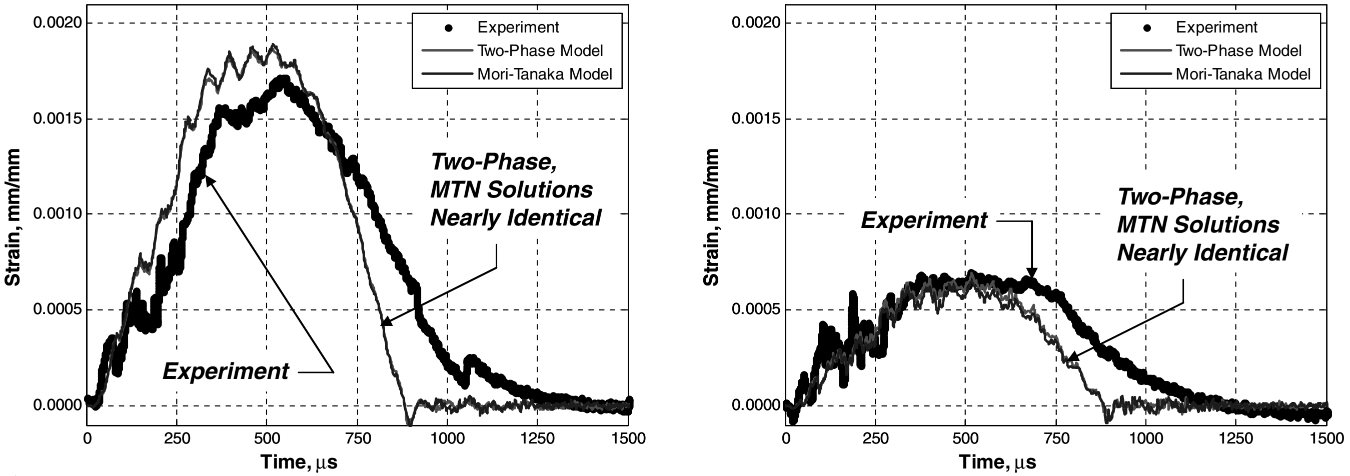

a) b)

Fig. 18 Test 9 strain histories vs FEM results: a) strain gauge 2, and b) strain gauge 3. Specimen was seven-layer FGM with an impact velocity of 3.765 m/s.

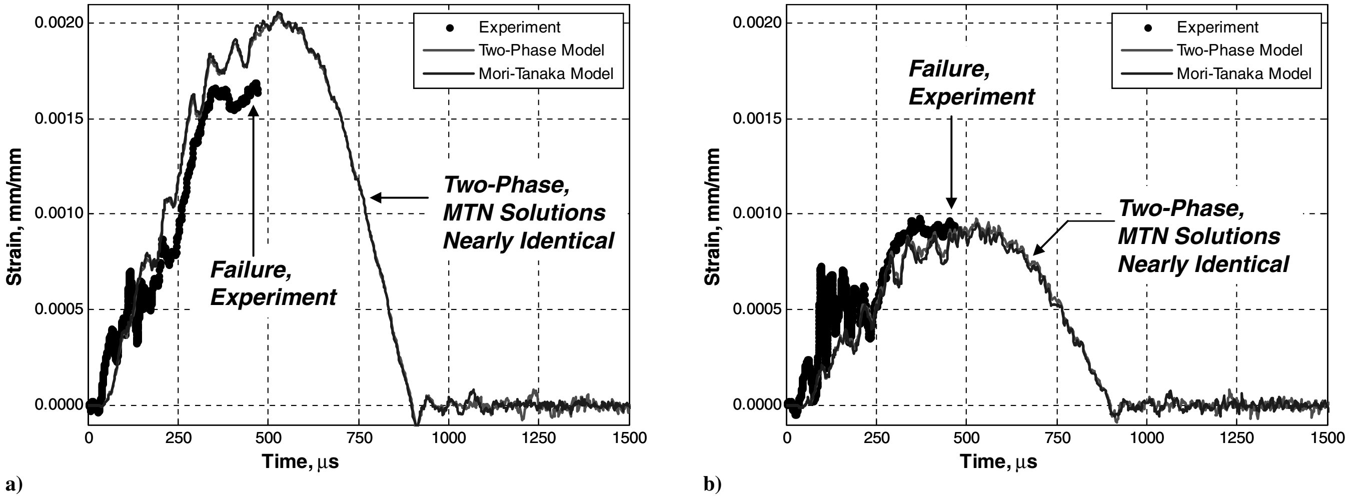

a) b)

Fig. 19 Test 10 strain histories vs FEM results: a) strain gauge 2, and b) strain gauge 3. Specimen was seven-layer FGM with an impact velocity of 4.078 m/s.

assume that failure will occur in the FGM under the conditions of test 10 in all cases would require more testing. No histories, experimental or simulated, are included for tests 5 and 6 due to the catastrophic failure of the plates.

As a reasonable correlation between the test results and the FEM strain histories was demonstrated, more detailed analysis can be presented. By simple inspection, it can be seen that there are many strong correlations between the FEMs and the test data, and there are also areas of discrepancy that need to be addressed. First, the FEMs can predict the peak maximum values of the strains for both gauges at both locations very effectively. In most cases, both the two-phase model and the homogenized-layer models are within a reasonable error of the test results (discussed in greater detail shortly). In some cases the two-phase and homogenized-layer models are nearly identical in response, and in other cases the maximum strain predicted is slightly greater or less than the counterpart. The two-phase model is generated by randomly distributing cells of Ti and TiB, and so it is not unexpected that this can and will occur.

Some of the test data show highly distinct and sharp oscillations very early in the response that disappear as the deflections become larger through the course of the impact event. These oscillations are not reflected in the FEM and are undoubtedly related to noise in the data or electrical shorting of the strain gauges (the fluttering of the single-stranded jumper wires during impact loading were found to account for this). The FEM clearly shows several vibration modes being excited upon impact from the tup. Some of these modes are not clearly discernible in the test results. On the other hand, it appears that there are some lower frequency modes being excited in the test data that are not reflected in the FEM, especially near the peaks of the response (especially gauge 2). This could be attributed to many possibilities, including error in applied material properties and the nature of the boundary conditions and constraints applied in the FEM. Addressing the former, Hill and Lin [42] reported material properties while testing Ti–TiB FGM specimens that were significantly lower than the properties predicted by Mori–Tanaka estimates or other similar models. This is partially due to the difficulty in controlling the exact volume fractions of Ti to TiB given that a chemical reaction is required to produce the TiB in situ, but may also be related to the sintering process itself. Additionally, the strain gauge adhesive may inherently damp out some of the oscillations that occur in the plate and are thus not registered in the strain histories from the tests. The histories from the finite element models are obtained from strain recorded directly from nodes in the vicinity of the strain gauge grids on the surface of the plate. Note that damping was not included in the FEM simulations presented here. Values for damping coefficients were not available for the Ti–TiB system at the time of this study. An informal study of the matter showed that the addition of artificial values of damping to the FEM significantly increased the computational cost of running the simulations with virtually no effect on the strain histories.

B. Maximum Strains During Impact

Tables 3–5 show the maximum value of strain from each experiment versus that predicted by the finite element models. In most cases, both the two-phase model and the homogenized-layer models are within a reasonable error of the test results. The majority of the tabulated strains from the FEM simulations are within approximately 10% of the experimental results. A few gauges have differences that are higher; the largest difference is shown to be 22% (found in test 4, gauge 3; see Table 5). Tests in which the plates and gauges failed are not tabulated.

Figure 20 shows a plot of the radial strain distribution in the FGM plate in test 8 at the point of maximum transverse deflection along the axes on the bottom surface of the plate where the strain gauges were installed. One plot shows the strain distributions along the two axes for the two-phase model, whereas the second plot shows the same strain distributions along the same axes using the homogenized-layers MTN model. Also shown (on separate plots for purposes of clarity) are the areas, or "windows," covered by each gauge based on the schematic in Fig. 1. It is very clear, simply from these FEM-based distributions, that the maximum radial strain varies significantly over the small area occupied by each gauge. For this reason, the nodes directly under each strain gauge grid were averaged to give the results plotted in Figs. 12–19. However, it is easy to see that small changes to the gauge grid location can significantly affect a strain history's maximum recorded value. This can account for some error between the histories and Tables 3–5.

Table 3 Maximum strain comparison between experiment and FEM results, strain gauge 1

Test no.	Plate specimen	Impact energy, J	Experiment max strain	Two-phase FEM, max strain	MTN FEM, max strain	Maximum percent difference
1	100% Ti, 0% TiB monolithic	60.35	Gauge failed	0.001943	0.001943	
2	100% Ti, 0% TiB monolithic	78.90	0.002602	0.002845	0.002845	9.33
3	85% Ti, 15% TiB monolithic	60.75	0.001711	0.001843	0.001684	7.70
4	85% Ti, 15% TiB monolithic	79.04	0.001764	0.001998	0.001833	13.21
5	15% Ti, 85% TiB monolithic	43.63	Plate Failed			
6	15% Ti, 85% TiB monolithic	60.75	Plate Failed			
7	Seven-layer Ti–TiB FGM	60.35	0.001459	0.001647	0.001621	12.82
8	Seven-layer Ti–TiB FGM	76.02	0.001783	0.001763	0.001737	−2.56
9	Seven-layer Ti–TiB FGM	92.56	0.001889	0.001894	0.001885	0.25
10	Seven-layer Ti–TiB FGM	108.6	Plate Failed	0.002071	0.002057	

Table 4 Maximum strain comparison between experiment and FEM results, strain gauge 2

Test no.	Plate specimen	Impact energy, J	Experiment max strain	Two-phase FEM, max strain	MTN FEM, max strain	Maximum percent difference
1	100% Ti, 0% TiB monolithic	60.35	0.001173	0.001131	0.001131	−3.54
2	100% Ti, 0% TiB monolithic	78.90	0.001161	0.001239	0.001239	6.69
3	85% Ti, 15% TiB monolithic	60.75	0.001603	0.001461	0.001679	−8.86
4	85% Ti, 15% TiB monolithic	79.04	0.001469	0.001581	0.001401	7.60
5	15% Ti, 85% TiB monolithic	43.63	Plate Failed			
6	15% Ti, 85% TiB monolithic	60.75	Plate Failed			
7	Seven-layer Ti–TiB FGM	60.35	0.001391	0.001227	0.001281	−11.78
8	Seven-layer Ti–TiB FGM	76.02	0.001468	0.001307	0.001358	−10.97
9	Seven-layer Ti–TiB FGM	92.56	0.001720	0.001867	0.001890	9.86
10	Seven-layer Ti–TiB FGM	108.6	Plate Failed	0.002045	0.002061	

Table 5 Maximum strain comparison between experiment and FEM results, strain gauge 3

Test no.	Plate specimen	Impact energy, J	Experiment max strain	Two-phase FEM, max strain	MTN FEM, max strain	Maximum percent difference
1	100% Ti, 0% TiB monolithic	60.35	0.0005157	0.0006026	0.0006026	16.86
2	100% Ti, 0% TiB monolithic	78.90	0.0009269	0.0009241	0.0009241	−0.31
3	85% Ti, 15% TiB monolithic	60.75	0.0008058	0.0009139	0.0007308	13.41
4	85% Ti, 15% TiB monolithic	79.04	0.0007834	0.0009579	0.0007774	22.27
5	15% Ti, 85% TiB monolithic	43.63	Plate Failed			
6	15% Ti, 85% TiB monolithic	60.75	Plate Failed			
7	Seven-layer Ti–TiB FGM	60.35	0.0006638	0.0006103	0.0005626	−15.24
8	Seven-layer Ti–TiB FGM	76.02	0.0007573	0.0006394	0.0008032	−15.56
9	Seven-layer Ti–TiB FGM	92.56	0.0007016	0.0006914	0.0006498	−7.39
10	Seven-layer Ti–TiB FGM	108.6	Plate Failed	0.0009787	0.0009522	

C. Strain Rates in Loading and Unloading

Strain rates are important to the discussion of nearly all impact events. Here the average strain rates in the plate from both the experiments and the FEMs will be compared using the homogenized-layers FGM model (the strain rates predicted by the two-phase FEM are virtually identical to the homogenized-layers FEM). The impact interaction between each plate and tup occurs over two significant periods of time: 1) a "loading" period, and 2) an "unloading" period. Figure 21 shows how the strain rates in loading and unloading in the experiments and FEMs are determined. A linear, least-squares curve fit to the data in the loading and unloading portions of the strain histories was applied. The linear data fit was used to determine a general slope to the line through the data. The slope of that line is the strain rate for that part of the curve. The strain rate is not, in general, a constant through the duration of the impact events. For each oscillation in the history, the strain rate is changing dynamically. However, the linear fit to the data in the loading and unloading portions of the curve allow general trends to be assessed. The line fit was taken so that the peak at maximum strain from each gauge was not included in the strain-rate calculation. The duration of the experimental histories was slightly longer than that of the FEMs and so the times over which the strain rates were assessed in the loading and unloading portions of the curves were adjusted accordingly.

Tables 6–9 show tabulated strain rates for the Dynatup and FEM impact tests for both loading and unloading at the three gauge locations. Also shown are the tup impact velocities for each of the tests for reference. In general, the strain rates show a trend in which increasing tup velocity results in an increasing magnitude of strain rate. This trend is not followed in all instances, but this can be attributed to the positioning of the gauges in the experiments, which can have a profound effect on the strain histories. Further, the FEM was used to match the experimental strain histories as close as possible and accounted for this potential variation in gauge placement. Note that the magnitudes of strain rates are, for the most part, lower the farther away the gauges are from the center. The strain histories at the gauge locations all reach maximum values at the same time, and the strain magnitude is dictated by the location of the gauge with respect to the center of the plate. Thus, gauges farther away from the center reach a lower magnitude of maximum strain at the same time instant as gauges closer to the center reach a larger magnitude of maximum strain. Because the strain rate is more or less the difference in strain divided by the time period the difference is measured, it is easy to see how the rates near the circular opening of the fixture would be less than those near the center of the plates.

The maximum *magnitude* of strain rate for any of the impact tests is 8.847 s^{-1} in the unloading of the pure titanium plate in test 2, predicted by the FEM. These rates of strain, as tabulated for these tests, are very low compared with what would be experienced from a high-speed impact, such as would occur from a projectile in space [43]. In applications such as these, the rates of strain can be in excess of 10^3–10^5. Given rates as high as these, localized wave response and

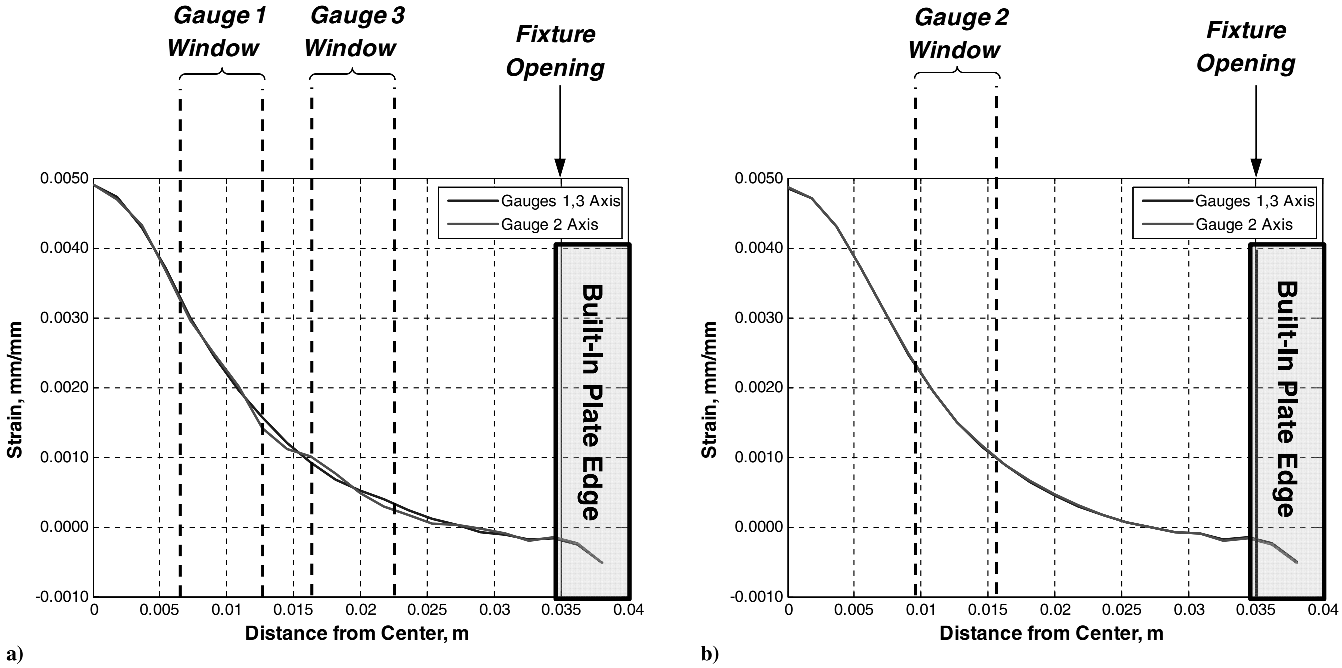

Fig. 20 Comparison of radial strain distribution along plate axes containing strain gauges on bottom surface of plate after impact at instant of maximum transverse deflection: a) two-phase model, and b) Mori–Tanaka homogenized-layers model. Specimen was seven-layer FGM with an impact velocity of 3.412 m/s (test 8).

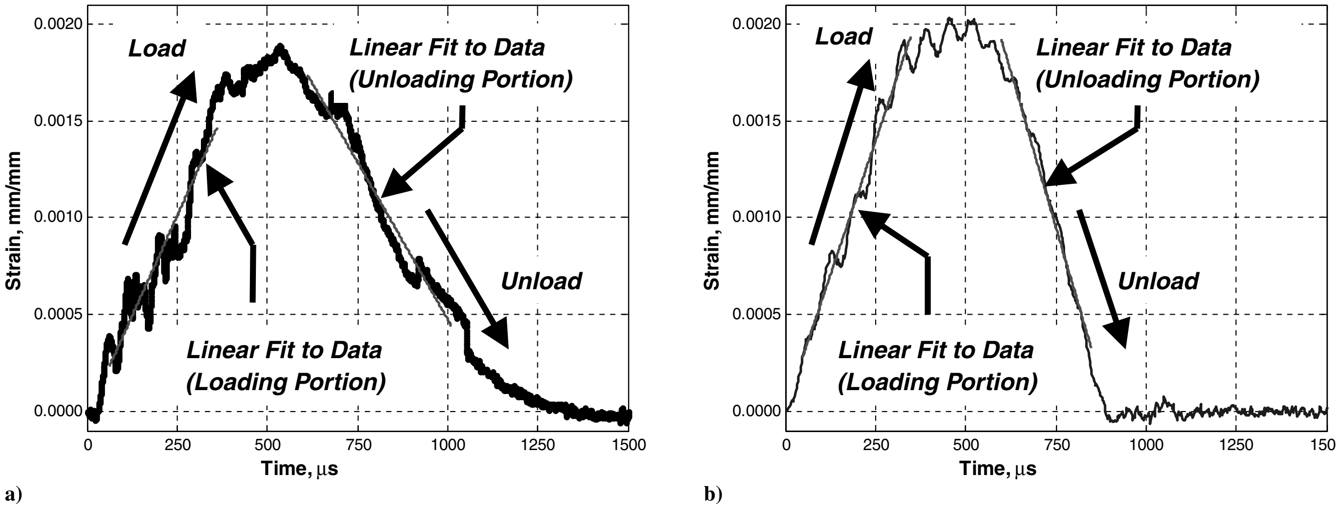

Fig. 21 A straight line was fit to the data in the loading and unloading portions of the strain history curves to determine the strain rates in each respective part of the curve. Shown are the data from FGM plate test 9, strain gauge 2: a) experimental, and b) FEM with homogenized-layers MTN model.

the effects of rate-sensitive constitutive models need to be included [43]. The rates experienced by the FGM plates here in these tests are low enough that the global effects dominate the solution, and the local wave effects are so dominated by the global response of the structure that they are virtually indistinguishable. The key conclusion based on this analysis is that elastic, rate-independent material properties are sufficient for studying the Ti–TiB FGMs under these impact loading conditions.

An interesting trend is that the magnitude of strain rate in the experiments is greater in the loading of the plate and lower in the unloading of the plate. Just the opposite is true with the FEMs. In the FEMs, the magnitude of strain rate is greater in the unloading than in the loading. The strain rates with respect to the loading of the plates experimentally and through the FEM show good correlation. The FEMs predict loading slopes (that is, strain rates) comparable to the experimental data for the gauges up to the point of maximum strain. As mentioned, the strain rates associated with each plate's unloading history do not correlate well. In fact, it appears that the rate the plate returns from maximum strain to "zero" strain is significantly less than that of the FEM. It is not likely that this behavior is associated with the monolithic or FGM composites themselves, indicating an invalid material model or FEM. One possibility is that it is an effect of the response of the adhesive used for the strain gauges unloading in a different manner than when it loads in tension to maximum strain. This effect could cause a measured strain different than the actual strain associated with the plate. This would additionally explain why gauges from the same specimen indicate larger or smaller windows for the total time over which the impact event occurs. Another explanation for the discrepancy is that the constraints and boundary conditions applied to the finite element model are too restrictive when compared with the actual tests. The constraints and boundary conditions in the FEM could cause the simulated plates to rebound

Table 6 Strain rate applied to plate during loading portion of impact event; experiment

			Strain rates, loading (1/s)		
Test no.	Plate specimen	Actual tup velocity, m/s	Gauge 1	Gauge 2	Gauge 3
1	100% Ti, 0% TiB monolithic	3.040	Gauge failed	2.184	0.967
2	100% Ti, 0% TiB monolithic	3.476	6.175	2.754	2.161
3	85% Ti, 15% TiB monolithic	3.050	3.979	3.302	1.800
4	85% Ti, 15% TiB monolithic	3.479	3.759	3.367	1.781
5	15% Ti, 85% TiB monolithic	2.585	Plate failed	Plate failed	Plate failed
6	15% Ti, 85% TiB monolithic	3.050	Plate failed	Plate failed	Plate failed
7	Seven-layer Ti–TiB FGM	3.040	2.509	2.467	1.110
8	Seven-layer Ti–TiB FGM	3.412	3.927	3.389	1.643
9	Seven-layer Ti–TiB FGM	3.765	4.135	4.091	1.379
10	Seven-layer Ti–TiB FGM	4.078	5.167	4.678	2.140

Table 7 Strain rate applied to plate during loading portion of impact event; FEM (MTN)

			Strain rates, loading (1/s)		
Test no.	Plate specimen	Actual tup velocity, m/s	Gauge 1	Gauge 2	Gauge 3
1	100% Ti, 0% TiB monolithic	3.040	4.295	2.374	1.162
2	100% Ti, 0% TiB monolithic	3.476	6.738	2.821	2.032
3	85% Ti, 15% TiB monolithic	3.050	4.035	4.055	1.640
4	85% Ti, 15% TiB monolithic	3.479	4.964	3.756	2.038
5	15% Ti, 85% TiB monolithic	2.585	Plate failed	Plate failed	Plate failed
6	15% Ti, 85% TiB monolithic	3.050	Plate failed	Plate failed	Plate failed
7	Seven-layer Ti–TiB FGM	3.040	4.099	3.152	1.272
8	Seven-layer Ti–TiB FGM	3.412	4.850	3.726	2.077
9	Seven-layer Ti–TiB FGM	3.765	5.527	4.261	1.724
10	Seven-layer Ti–TiB FGM	4.078	5.852	4.507	2.508

Table 8 Strain rate applied to plate during unloading portion of impact event; experiment

			Strain rates, loading (1/s)		
Test no.	Plate specimen	Actual tup velocity, m/s	Gauge 1	Gauge 2	Gauge 3
1	100% Ti, 0% TiB monolithic	3.040	Gauge failed	−2.111	−0.363
2	100% Ti, 0% TiB monolithic	3.476	−4.463	−1.746	−1.589
3	85% Ti, 15% TiB monolithic	3.050	−2.966	−2.393	−1.331
4	85% Ti, 15% TiB monolithic	3.479	−3.207	−2.580	−1.350
5	15% Ti, 85% TiB monolithic	2.585	Plate failed	Plate failed	Plate failed
6	15% Ti, 85% TiB monolithic	3.050	Plate failed	Plate failed	Plate failed
7	Seven-layer Ti–TiB FGM	3.040	−2.449	−2.074	−1.096
8	Seven-layer Ti–TiB FGM	3.412	−3.522	−2.432	−1.723
9	Seven-layer Ti–TiB FGM	3.765	−3.245	−3.599	−1.477
10	Seven-layer Ti–TiB FGM	4.078	Plate failed	Plate failed	Plate failed

Table 9 Strain rate applied to plate during unloading portion of impact event; FEM (MTN)

			Strain rates, loading (1/s)		
Test no.	Plate specimen	Actual tup velocity, m/s	Gauge 1	Gauge 2	Gauge 3
1	100% Ti, 0% TiB monolithic	3.040	−5.862	−3.283	−1.604
2	100% Ti, 0% TiB monolithic	3.476	−8.847	−3.764	−2.682
3	85% Ti, 15% TiB monolithic	3.050	−4.879	−4.904	−1.975
4	85% Ti, 15% TiB monolithic	3.479	−5.498	−4.164	−2.231
5	15% Ti, 85% TiB monolithic	2.585	Plate failed	Plate failed	Plate failed
6	15% Ti, 85% TiB monolithic	3.050	Plate failed	Plate failed	Plate failed
7	Seven-layer Ti–TiB FGM	3.040	−5.368	−4.119	−1.608
8	Seven-layer Ti–TiB FGM	3.412	−6.006	−4.620	−2.548
9	Seven-layer Ti–TiB FGM	3.765	−6.397	−4.906	−1.898
10	Seven-layer Ti–TiB FGM	4.078	Plate failed	Plate failed	Plate failed

more quickly than the actual plates while simultaneously neglecting friction and leveraging effects that could slow the unloading response of the plate.

V. Conclusions

In this paper, the response of functionally graded materials subject to impact loading has been considered. A titanium–titanium-boride metal–ceramic composite system was chosen for a series of plate impact experiments. Strain histories were successfully collected from the impact experiments. The test results were compared with finite element simulations using two-phased and homogenized-layer material models to emulate the material properties of the Ti–TiB monolithic and graded plates. The FEM simulations compared well with the experimental data, and some inferences about differences between the test results and simulations were made. *The key conclusion* of this work is that the two-phase and homogenized-layer material models appear to be adequate for studying elastic FGM plate dynamics and work well within the more general finite element framework as demonstrated by the correlation between experiment and simulation. The *major contribution* of this work is the validation of FGM material models and a computational framework for studying the impact response of FGM plates as a foundation for investigations of more severe impact loads at higher velocities and energy levels.

The greatest challenge in working with FGMs is determining accurate and consistent material properties for the mixture of materials. This is especially true with a metal–ceramic combination. The finite element methods used to analyze the impact responses of FGM specimens worked very well overall but undoubtedly could have improved with more knowledge of the basic properties of the layers in the FGMs. The powder sintering process used to construct the materials also adds complexity as the microstructure of sintered materials is of an inherently different nature than wrought materials or even many other metal-matrix composites. Until more accurate material characterizations are available, the general two-phase and homogenized-layer material models are adequate for studying dynamic loading in the elastic regime.

Acknowledgments

The views expressed in this article are those of the authors and do not reflect the official policy or position of the U.S. Air Force, Department of Defense, or the U.S. Government. This work was funded by the U.S. Air Force Research Laboratory, Air Vehicles Directorate, Structural Science Center (AFRL/RBS); and the Dayton Area Graduate Studies Institute (DAGSI) under the AFRL/DAGSI Ohio Student–Faculty Research Fellowship Program. The authors would like to further acknowledge Brian Smyers, Richard Wiggins, and Brett Hauber (AFRL/RBS); Daniel Ryan (U.S. Air Force Institute of Technology); Kevin Poormon (University of Dayton Research Institute); and Rachael DeRoche (Pennsylvania State University) and Joe Sabat (U.S. Air Force Academy) for their various contributions to this research.

References

[1] Suresh, S., and Mortensen, A., *Fundamentals of Functionally Graded Materials: Processing and Thermomechanical Behaviour of Graded Metals and Metal-Ceramic Composites*, IOM Communications, Ltd.,, Cambridge, UK, 1998.

[2] Birman, V., and Byrd, L. W., "Modeling and Analysis of Functionally Graded Materials and Structures," *Applied Mechanics Reviews*, Vol. 60, 2007, pp. 195–216.
doi:10.1115/1.2777164

[3] Lambros, J., Santare, M. H., Li, H., and Sapna, G. H., III, "A Novel Technique for the Fabrication of Laboratory Scale Functionally Graded Materials," *Experimental Mechanics*, Vol. 39, No. 3, 1999, pp. 184–190.
doi:10.1007/BF02323551

[4] Lambros, J., Narayanaswamy, A., Santare, M. H., and Anlas, G., "Manufacture and Testing of a Functionally Graded Material," *Journal of Engineering Materials and Technology*, Vol. 121, 1999, pp. 488–493.
doi:10.1115/1.2812406

[5] Parameswaran, V., and Shukla, A., "Processing and Characterization of a Model Functionally Gradient Material," *Journal of Materials Science*, Vol. 35, 2000, pp. 21–29.
doi:10.1023/A:1004767910762

[6] Reddy, J. N., Wang, C. M., and Kitipornchai, S., "Axisymmetric Bending of Functionally Graded Circular and Annular Plates,"

European Journal of Mechanics. A, Solids, Vol. 18, 1999, pp. 185–199. doi:10.1016/S0997-7538(99)80011-4

[7] Reddy, J. N., "Analysis of Functionally Graded Plates," *International Journal for Numerical Methods in Engineering*, Vol. 47, 2000, pp. 663–684. doi:10.1002/(SICI)1097-0207(20000110/30)47:1/3<663::AID-NME787>3.0.CO;2-8

[8] Reddy, J. N., and Cheng, Z. Q., "Three-Dimensional Thermomechanical Deformations of Functionally Graded Rectangular Plates," *European Journal of Mechanics. A, Solids*, Vol. 20, No. 5, 2001, pp. 841–860.

[9] Reddy, J. N., and Cheng, Z. Q., "Frequency Correspondence Between Membranes and Functionally Graded Spherical Shallow Shells of Polygonal Planform," *International Journal of Mechanical Sciences*, Vol. 44, No. 5, 2002, pp. 967–985. doi:10.1016/S0020-7403(02)00023-1

[10] Loy, C. T., Lam, K. Y., and Reddy, J. N., "Vibration of Functionally Graded Cylindrical Shells," *International Journal of Mechanical Sciences*, Vol. 41, No. 3, 1999, pp. 309–324. doi:10.1016/S0020-7403(98)00054-X

[11] Pradhan, S. C., Loy, C. T., Lam, K. Y., and Reddy, J. N., "Vibration Characteristics of Functionally Graded Cylindrical Shells Under Various Boundary Conditions," *Applied Acoustics*, Vol. 61, 2000, pp. 111–129. doi:10.1016/S0003-682X(99)00063-8

[12] Woo, J., and Meguid, S. A., "Nonlinear Analysis of Functionally Graded Plates and Shallow Shells," *International Journal of Solids and Structures*, Vol. 38, 2001, pp. 7409–7421. doi:10.1016/S0020-7683(01)00048-8

[13] Yang, J., and Shen, H. -S., "Dynamic Response of Initially Stressed Functionally Graded Rectangular Thin Plates," *Composite Structures*, Vol. 54, 2001, pp. 497–508. doi:10.1016/S0263-8223(01)00122-2

[14] Yang, J., and Shen, H.-S., "Vibration Characteristics and Transient Response of Shear Deformable Functionally Graded Plates in Thermal Environments," *Journal of Sound and Vibration*, Vol. 255, No. 3, 2002, pp. 579–602. doi:10.1006/jsvi.2001.4161

[15] Vel, S. S., and Batra, R. C., "Exact Solution for Thermoelastic Deformations of Functionally Graded Thick Rectangular Plates," *AIAA Journal*, Vol. 40, No. 7, 2002, pp. 1421–1433. doi:10.2514/2.1805

[16] Prakesh, T., and Ganapathi, M., "Axisymmetric Flexural Vibration and Thermoelastic Stability of FGM Circular Plates Using Finite Element Method," *Composites. Part B, Engineering*, Vol. 37, 2006, pp. 642–649. doi:10.1016/j.compositesb.2006.03.005

[17] Gong, S. W., Lam, K. Y., and Reddy, J. N., "The Elastic Response of Functionally Graded Cylindrical Shells to Low-Velocity Impact," *International Journal of Impact Engineering*, Vol. 22, No. 4, 1999, pp. 397–417.

[18] Bruck, H. A., "A One-Dimensional Model for Designing Functionally Graded Materials to Manage Stress Waves," *International Journal of Solids and Structures*, Vol. 37, 2000, pp. 6383–6395. doi:10.1016/S0020-7683(99)00236-X

[19] Li, Y., Ramesh, K. T., and Chin, E. S. C., "Dynamic Characterization of Layered and Graded Structures Under Impulsive Loading," *International Journal of Solids and Structures*, Vol. 38, 2001, pp. 6045–6061. doi:10.1016/S0020-7683(00)00364-4

[20] Banks-Sills, L., Eliasi, R., and Berlin, Y., "Modeling of Functionally Graded Materials in Dynamic Analyses," *Composites. Part B, Engineering*, Vol. 33, 2002, pp. 7–15. doi:10.1016/S1359-8368(01)00057-9

[21] Decker, B. F., and Kasper, J. S., "The Crystal Structure of TiB," *Acta Crystallographica*, Vol. 7, 1954, pp. 77–80. doi:10.1107/S0365110X5400014X

[22] Sahay, S. S., Ravichandran, K. S., and Atri, R., "Evolution of Microstructure and Phases In Situ Processed Ti–TiB Composites Containing High Volume Fractions of TiB Whiskers," *Journal of Materials Research*, Vol. 14, No. 11, 1999, pp. 4214–4223. doi:10.1557/JMR.1999.0571

[23] Atri, R., Ravichandran, K. S., and Jha, S. K., "Elastic Properties of In-Situ Processed Ti–TiB Composites Measured By Impulse Excitation of Vibration," *Materials Science and Engineering A*, Vol. 271, 1999, pp. 150–159. doi:10.1016/S0921-5093(99)00198-7

[24] Panda, K. B., and Ravichandran, K. S., "First Principles Determination of Elastic Constants and Chemical Bonding of Titanium Boride (TiB) on the Basis of Density Functional Theory," *Acta Materiala*, Vol. 54, 2006, pp. 1641–1657.

[25] Panda, K. B., and Ravichandran, K. S., "Synthesis of Ductile Titanium–Titanium Boride (Ti–TiB) Composites with Beta-Titanium Matrix: The Nature of TiB Formation and Composite Properties," *Metallurgical and Materials Transactions A: Physical Metallurgy and Materials Science*, Vol. 34, 2003, pp. 1371–1385. doi:10.1007/s11661-003-0249-z

[26] Ravichandran, K. S., Panda, K. B., and Sahay, S. S., "A TiBw-Reinforced Ti Composite: Processing, Properties, Application Prospects, and Research Needs," *JOM The Journal of the Minerals, Metals and Materials Society*, Vol. 56, No. 5, 2004, pp. 42–48. doi:10.1007/s11837-004-0127-1

[27] Cleveland, W. S., "Robust Locally Weighted Regression and Smoothing Scatterplots," *Journal of the American Statistical Association*, Vol. 74, No. 368, 1979, pp. 829–836. doi:10.2307/2286407

[28] Cleveland, W. S., and Devlin, S. J., "Locally Weighted Regression: An Approach to Regression Analysis by Local Fitting," *Journal of the American Statistical Association*, Vol. 83, No. 403, 1988, pp. 596–610. doi:10.2307/2289282

[29] ABAQUS, Software Package, Ver. 6.6-1, Dassault Systèmes SIMULIA, Providence, RI, 2008.

[30] Oberg, E., Jones, F. D., Horton, H. L., and Ryfell, H. H. (eds.), *Machinery's Handbook*, 26th Ed., Industrial Press, Inc., New York, NY, 2000.

[31] Daniel, I. M., and Ishai, O., *Engineering Mechanics of Composite Materials*, 2nd ed., Oxford Univ. Press, New York, 2006.

[32] Hill, R., "A Self-Consistent Mechanics of Composite Materials," *Mechanics of Composite Materials*, Vol. 13, 1965, pp. 213–222.

[33] Hashin, Z., and Shtrikman, S., "A Variational Approach to the Theory of the Elastic Behaviour of Multiphase Materials," *Journal of the Mechanics and Physics of Solids*, Vol. 11, 1963, pp. 127–140. doi:10.1016/0022-5096(63)90060-7

[34] Hashin, Z., "Assessment of the Self-Consistent Scheme Approximation: Conductivity of Particulate Composites," *Journal of Composite Materials*, Vol. 2, No. 3, 1968, pp. 284–300. doi:10.1177/002199836800200302

[35] Yin, H. M., Paulino, G. H., Buttlar, W. G., and Sun, L. Z., "Micromechanics-Based Thermoelastic Model for Functionally Graded Particulate Materials with Particle Interactions," *Journal of the Mechanics and Physics of Solids*, Vol. 55, 2007, pp. 132–160. doi:10.1016/j.jmps.2006.05.002

[36] Mori, T., and Tanaka, K., "Average Stress in Matrix and Average Elastic Energy of Materials with Misfitting Inclusions," *Acta Metallurgica*, Vol. 21, 1973, pp. 571–574. doi:10.1016/0001-6160(73)90064-3

[37] Benveniste, Y., "A New Approach to the Application of Mori–Tanaka's Theory in Composite Materials," *Mechanics of Materials*, Vol. 6, 1987, pp. 147–157. doi:10.1016/0167-6636(87)90005-6

[38] Berryman, J. G., "Long-Wavelength Propagation in Composite Elastic Media I: Spherical Inclusions," *Journal of the Acoustical Society of America*, Vol. 68, No. 6, 1980, pp. 1809–1819. doi:10.1121/1.385171

[39] Berryman, J. G., "Long-Wavelength Propagation in Composite Elastic Media II: Ellipsoidal Inclusions," *Journal of the Acoustical Society of America*, Vol. 68, No. 6, 1980, pp. 1820–1831. doi:10.1121/1.385172

[40] Belytschko, T., Liu, W. K., and Moran, B., *Nonlinear Finite Elements for Continua and Structures*, Edward Arnold, Ltd., London, 1960.

[41] ABAQUS Theory Manual, ABAQUS Software Package, Ver. 6.6, Dassault Systèmes SIMULIA, Providence, RI, 2008.

[42] Hill, M. R., and Lin, W., "Residual Stress Measurement in a Ceramic-Metallic Graded Material," *Journal of Engineering Materials and Technology*, Vol. 124, 2002, pp. 185–191. doi:10.1115/1.1446073

[43] Zukas, J. A., Nicholas, T., Swift, H. F., Greszczuk, L. B., and Curran, D. R., *Impact Dynamics*, Wiley, New York, NY, 1982.